Geometrically exact 3D arbitrarily curved rod theory for dynamic analysis: Application to predicting the motion of hard-magnetic soft robotic arm

Xin Li, Wenkai Yu, Xiaoyan Zhu, Ju Liu, Hongyan Yuan [*]

Department of Mechanics and Aerospace Engineering, Southern University of Science and Technology, Shenzhen, Guangdong 518055, China

ABSTRACT

Magnetorheological elastomers are active materials which can be actuated by the applied magnetic field. Hard magnetic soft (HMS) materials, a type of magnetorheological elastomers, show great potential in the fields of biomedical engineering and soft robotics, due to their short response time, remote operation, and shape programmability. To exploit its potential, a series of theoretical frameworks of HMS rods have been developed, but they are mainly limited to the static rod models or classical curved rod models that fail to consider the effect of the "initial curvature" on the distribution of the stress. In this work, we develop a curved rod theory to predict the 3D dynamic motion of the rod-like HMS robotics under large deformation. Based on the geometrically exact rod theory, we include the heterogeneous initial length of the longitudinal fiber caused by "initial curvature" into our model and obtain the reduced balance equations of the HMS robotics. As a result, the "tension-bending" and "shear-torsion" coupling effects of curved rods emerge in the present model. A numerical implementation of our model based on the classical Newmark algorithm is presented. To validate our model, three numerical examples, including the dynamic snap-through behavior of a bistable arch, are performed and compared with the simulation or experiment results reported in literatures, which show a good agreement. Finally, we experimentally study the 2D and 3D static and dynamic motion of a quarter arc HMS robotic arm under an applied magnetic field of 10 mT, and our model gives a satisfactory prediction, especially for static deformation.

1. Introduction

Magnetorheological elastomers are a type of active soft materials which can deform under the applied magnetic field. Due to their short response time, wireless control, and superior performance in closed space, magnetorheological elastomers exhibit enormous potential in the field of biomedical engineering [1,2]. In recent years, hard magnetic soft (HMS) materials, a kind of magneto-rheological elastomers that possess high coercivity and high remanence, have attracted the interest of researchers [3]. HMS materials commonly are fabricated by mixing the soft matrices and the embedded hard-magnetic particles, such as NdFeB magnets [4–6]. The high remanence of the HMS materials allows them to achieve complex and programmable deformation, which is attractive to the fields of soft robotics, sensors, biomedical devices, and microfluidic devices [7]. Many hard-magnetic soft robotics have been developed in

---

the past decade. Wang et al. [8] designed a magnetic continuum robot with different deformation modes under the magnetic fields in different directions for vascular interventional navigation surgery. Diller et al. [9] presented a magnetic swimming robot with the heterogeneous residual magnetic flux density distribution. Lum et al. [10] proposed a universal programming methodology for the shape -programmable magnetic soft actuators, and created some biomimetic robots based on the method. A magnetic soft continuum robot which can navigate through a 3D cerebrovascular phantom network have been developed by Kim et al. [11]. In addition, a series of interesting applications of HMS materials have been developed, such as the magnetic nanocomposite tactile sensor [12], the tunable metamaterials triggered by magnetic field [13–15], and the magnetic polymers for magnetophoretic separation in microfluidic devices [16].

To further exploit the potential of the HMS materials, it is necessary to develop the mechanics model to predict their deformation [17]. In a top-down approach, Zhao et al. [18] presented a decoupled model for the pre-magnetized HMS materials. In their work, the unaltered applied magnetic flux density and the linear relation between the magnetic field and magnetic flux density were assumed to obtain a simple and concise magnetic Helmholtz free energy. Furthermore, the dipole–dipole interactions and the heterogeneous pre-magnetization distribution were ignored in their model. Despite the limitations, their model showed desirable predictive capability for slender structures under small applied magnetic fields. The viscoelastic effect of the HMS material was analyzed by Garcia-Gonzalez et al. [19,20] and Stewart et al. [21]. To avoid the asymmetric stress tensor induced by the magnetic torque, Dadgar-Rad and Hossain [22] presented a model based on the micropolar continuum theory for the HMS materials. Different from the aforementioned continuum-based macroscopic model, some HMS mechanics models have been developed based on the microstructural approach [23–25] or the lattice model [26]. In addition, Mukherjee et al. [27,28] presented a thermodynamically consistent modeling framework for most isotropic magnetorheological elastomers (both soft-magnetic and hard-magnetic soft materials). In their work [27,29], the magnetic Helmholtz free energy presented by Zhao et al. [18], which is assumed to be modulated by the deformation gradient, was demonstrated to be not sufficiently accurate for large strains. The magnetic Helmholtz free energy should be stretch-independent and vary only with rotation. In our previous work [30], we modified the magnetic Helmholtz free energy by replacing the deformation gradient with an affine rotation in the formula to address the issue. Although, these continuum-based models can accurately predict the deformation of the HMS materials, the simulations of the complex HMS structures were still time-consuming.

For HMS robotics, an efficient computational model is desirable. Therefore, a series of mechanics models of the HMS rods, which are common structures in HMS robotics, have been developed. Wang et al. [31] and Arockiarajan et al. [32] focused on the one-dimensional bending deformation of the HMS beam, and the obtained results agreed well with previous experimental data. Chen et al. [33–35] theoretically investigated the 2D deformation of the non-uniformly magnetized HMS beam under constant magnetic field. In addition, Dadgar-Rad and Hossain [36] discussed the viscoelastic effect on the HMS beam. The buckling problem of the HMS cantilevers was investigated by Dehrouyeh-Semnani [37]. Very recently, some three-dimensional HMS rod models were developed. Based on the principle of minimum potential energy, Wang et al. [38] studied the 3D deformation of non-uniformly magnetized HMS rods in detail. Sano et al. [39] developed a 3D Kirchhoff HMS rod model, in which the spatially varying magnetic fields have been regraded. In the two works, the Euler angles are utilized to describe the 3D finite rotations in implementations. Dadgar-Rad et al. [40] presented a three-dimensional micropolar beam model to analyze the finite deformation of the HMS rod. Li et al. [30] investigated the effect of the cross-section deformation and hyperelasticity on the HMS rod. It should be mentioned that all the aforementioned works are limited to the static deformation of the HMS rod. The studies on the dynamic response of the HMS rod are rare, especially the 3D dynamic response. Chen et al. [41] presented a 2D dynamical curved beam model and investigated its vibration in detail. Dehrouyeh-Semnani [42] studied the magneto-hydro-elastic responses of a 2D fluid-conveying cantilevered hard magnetic soft pipe. Huang et al. [43,44] presented a 3D discrete dynamical model for the HMS slender structures and applied it to the simulation of the cilia carpet robots. In the present work, we analyze the 3D deformation of the HMS rod based on the geometrically exact rod theory in which only the rigid cross-section assumption is required. Compared to the aforementioned models, the present model does not ignore the shear deformation of the rod. It means that the present model will be more accurate in the case where the rod subjected to the load besides magnetic moment, such as gravity, especially for thick rod. In addition, the effect of "initial curvature" on the stress distribution of the cross-section was not considered in the three other models. In fact, due to the "initial curvature", the initial length of the longitudinal fiber is not constant. As a result, there exist the "tension-bending" coupling and "shear-torsion" coupling effects on the curved rod. Ignoring these effects is appropriate for "small-curvature" rods, however, it will make the model inaccurate when the "initial curvature" is significant [45]. Therefore, we investigate a 3D dynamical arbitrarily curved rod model in which the "tension-bending" coupling and "shear-torsion" coupling effects are considered based on the geometrically exact theory.

The curved rod model can be traced back to the work by Reissner and Simo [46–48], in which only the assumption of rigid cross-sections was applied. This model commonly is referred to as the "Simo-Reissner theory" or "geometrically exact rod model". If the shear effect is further ignored, the "Bernoulli–Euler theory" will be recovered, which is also usually called "Kirchhoff–Love theory". A series of numerical implementations [48–53] of the geometrically exact curved rod models and the Kirchhoff curved thin model have been developed recently. However, the "tension-bending" coupling and "shear-torsion" coupling effects have not been incorporated in the aforementioned models. The truly geometrically exact curved/twisted rods were discussed by Reissner [54] and Kapania et al. [55]. In their work, a general framework to obtain the constitutive relations of the curved rod was presented. However, the explicit relation between the elasticity constants and the classical cross-section characteristics, such as "moment of inertia", was not obtained. To address this issue, Borkovi et al. [45,56–60] developed the concise and explicit constitutive relations of the Kirchhoff curved thin rods. However, only static deformation is considered in it. To the best of our knowledge, the dynamic analysis of the geometrically exact curved rod with the "initial curvature" and "initial shear" effects taken into account has not been studied in detail in the literature. As we know, understanding the dynamic responses of the HMS rod, such as nonlinear vibrations, is important for the application of the HMS rod (e.g., locomotion control of the HMS robotics). For most HMS robotics, the straight HMS rods are not

enough to meet requirements. Therefore, it is necessary to develop a 3D arbitrarily curved rod dynamical theory for HMS robotics.

The article is organized as follows. First, in Section 2, we formulate the constitutive relations and the governing equations of the curved HMS rods. And then, the temporal and spatial discretization of the problem are presented in Section 3, to obtain the finite element formulation of the problem. In Section 4, three numerical examples, including the dynamic snap-through behavior of a bistable arch [61], are presented and compared with the results reported in the literature to validate our model. In Section 5, some experiments about the dynamic motion of a quarter arc HMS robotic arm, including the 3D dynamic motion, are presented, and the experiment results show good agreement with the simulation results. Finally, we summarize our work and discuss the limitations of our model in Section 6.

2. Formulation

This section first focuses on the geometric description and the constitutive relations of the curved HMS rods and then presents the governing equations for the dynamic analysis.

2.1. Geometric description

In the beginning, we introduce a Cartesian coordinate system defined by the orthonormal basis $\{e_i\}$ and the origin O as the fixed coordinate system. A typical curved rod shown in Fig. 1 can be considered as a non-denumerable set of cross-sections whose geometry centroids are connected by a curve referred to as the line of centroids. Every cross-section is marked by the curvilinear coordinate along the line of centroids on the undeformed configuration $S \in [0, L]$, where L is the total arc length of the undeformed rod. The Einstein summation convention is applied in this work for the dummy indices $i = 1, 2, 3$ and $\eta = 1, 2$. With the rigid cross-section assumption, the position vectors of the material point in the undeformed configuration x_0 and the deformed configuration x can be, respectively, expressed by

$$
\begin{aligned}
&x_0(S, \xi_1, \xi_2) = r_0(S) + \xi_\eta E_\eta(S) = r_0(S) + \xi_\eta \Lambda_0(S) e_\eta, \\
&x(S, \tau, \xi_1, \xi_2) = r(S, \tau) + \xi_\eta t_\eta(S, \tau) = r(S, \tau) + \xi_\eta \Lambda(S) e_\eta,
\end{aligned}
\tag{1}
$$

where r_0 and r are the position vectors of the centroids in the undeformed and deformed configurations; ξ_1 and ξ_2 are the components of the principal axis directions of the distance between the material point and the centroid; τ is the time coordinate; E_η and t_η are the unit vectors parallel to the centroid principal axis direction in the undeformed and deformed configurations. Thus, we can define two orthonormal frames $\{E_i\}$ and $\{t_i\}$ referred to as "material frame", where $E_3 = E_1 \times E_2$ and $t_3 = t_1 \times t_2$. Λ_0 and Λ are the orthogonal transformations between the material frames and the fixed frames, and can be expressed as
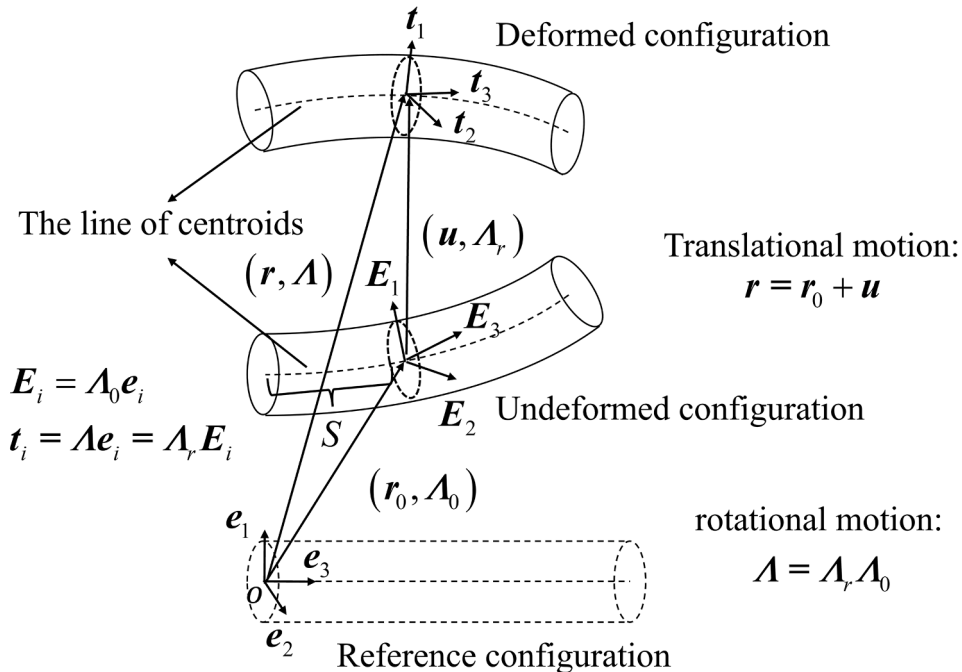

Fig. 1. Schematic of motion from the undeformed rod configuration to the deformed rod configuration. Three orthonormal frames are fixed frame $\{e_i\}$, material frame in the undeformed configuration $\{E_i\}$ and material frame in the deformed configuration $\{t_i\}$.

$$\Lambda_0 = \boldsymbol{E}_i \otimes \boldsymbol{e}_i \Rightarrow \boldsymbol{E}_i = \Lambda_0 \boldsymbol{e}_i,$$
$$\Lambda = \boldsymbol{t}_i \otimes \boldsymbol{e}_i \Rightarrow \boldsymbol{t}_i = \Lambda \boldsymbol{e}_i. \tag{2}$$

Therefore, the deformation of the rod can be described by the rigid motion of the family of cross-sections as

$$\boldsymbol{r}(S, \tau) = \boldsymbol{r}_0(S) + \boldsymbol{u}(S, \tau),$$
$$\Lambda(S, \tau) = \Lambda_r(S, \tau)\Lambda_0(S), \tag{3}$$

where $\boldsymbol{u}$ is the displacement of the centroids, and Λ_r is the rotational matrix of the cross-sections. In particular, it can be expressed as

$$\Lambda_r = \boldsymbol{t}_i \otimes \boldsymbol{E}_i \Rightarrow \boldsymbol{t}_i = \Lambda_r \boldsymbol{E}_i. \tag{4}$$

To further study the deformation of the curved rod, we formally introduce a virtual configuration referred to as "reference configuration", which is a straight rod with a length of L along the $\boldsymbol{e}_3$ direction, and the position vectors of the material points in the reference configuration $\boldsymbol{X}$ can be expressed as

$$\boldsymbol{X}(S, \xi_1, \xi_2) = S\boldsymbol{e}_3 + \xi_\eta \boldsymbol{e}_\eta. \tag{5}$$

The study of the deformation gradients is the key point to determine the constitutive relations of the curved rod. The deformation gradients of the undeformed configuration $\boldsymbol{F}_0$ and the deformed configuration $\boldsymbol{F}$ relative to the reference configuration can be given by

$$\boldsymbol{F}_0 = \frac{\partial \boldsymbol{x}_0}{\partial S} \otimes \boldsymbol{e}_3 + \frac{\partial \boldsymbol{x}_0}{\partial \xi_\eta} \otimes \boldsymbol{e}_\eta = \frac{\partial \boldsymbol{r}_0}{\partial S} \otimes \boldsymbol{e}_3 + \xi_\eta \frac{\partial \boldsymbol{E}_\eta}{\partial S} \otimes \boldsymbol{e}_3 + \boldsymbol{E}_\eta \otimes \boldsymbol{e}_\eta,$$
$$\boldsymbol{F} = \frac{\partial \boldsymbol{x}}{\partial S} \otimes \boldsymbol{e}_3 + \frac{\partial \boldsymbol{x}}{\partial \xi_\eta} \otimes \boldsymbol{e}_\eta = \frac{\partial \boldsymbol{r}}{\partial S} \otimes \boldsymbol{e}_3 + \xi_\eta \frac{\partial \boldsymbol{t}_\eta}{\partial S} \otimes \boldsymbol{e}_3 + \boldsymbol{t}_\eta \otimes \boldsymbol{e}_\eta. \tag{6}$$

The derivatives of the position vector can be expressed as

$$\frac{\partial \boldsymbol{r}_0}{\partial S} = \Gamma_{01}\boldsymbol{E}_1 + \Gamma_{02}\boldsymbol{E}_2 + \sqrt{1 - \left(\Gamma_{01}^2 + \Gamma_{02}^2\right)}\boldsymbol{E}_3 \approx \Gamma_{01}\boldsymbol{E}_1 + \Gamma_{02}\boldsymbol{E}_2 + \boldsymbol{E}_3,$$
$$\frac{\partial \boldsymbol{r}}{\partial S} = \Gamma_1 \boldsymbol{t}_1 + \Gamma_2 \boldsymbol{t}_2 + (\Gamma_3 + 1)\boldsymbol{t}_3, \tag{7}$$

where Γ_{01} and Γ_{02} are the "initial shear", Γ_1 and Γ_2 are the "total shear", and Γ_3 is the "total tension". The expression indicates the "initial tension" $\Gamma_{03} = \sqrt{1 - \left(\Gamma_{01}^2 + \Gamma_{02}^2\right)} - 1 \approx 0$, which is due to the length of the reference configuration is equal to the undeformed configuration. The derivative of the material frames can be defined as

$$\frac{\partial \boldsymbol{E}_i}{\partial S} = \boldsymbol{\omega}_0 \times \boldsymbol{E}_i = (\omega_{01}\boldsymbol{E}_1 + \omega_{02}\boldsymbol{E}_2 + \omega_{03}\boldsymbol{E}_3) \times \boldsymbol{E}_i, \quad \boldsymbol{\omega}_0^\wedge = \frac{\partial \Lambda_0}{\partial S}\Lambda_0^T,$$
$$\frac{\partial \boldsymbol{t}_i}{\partial S} = \boldsymbol{\omega} \times \boldsymbol{t}_i = (\omega_1 \boldsymbol{t}_1 + \omega_2 \boldsymbol{t}_2 + \omega_3 \boldsymbol{t}_3) \times \boldsymbol{t}_i, \quad \boldsymbol{\omega}^\wedge = \frac{\partial \Lambda}{\partial S}\Lambda^T, \tag{8}$$

where $\boldsymbol{\omega}_0$ is the "initial curvature", and ω_{0i} are the components of the initial curvature; $\boldsymbol{\omega}$ is the "total curvature", and ω_i are the components of the total curvature; $(\bullet)^\wedge$ represents the corresponding skew-symmetric tensor of the vector $(\bullet)$. Substituting Eqs. (7) and (8) into Eq. (6), the deformation gradients can be expressed as

$$\boldsymbol{F}_0 = \begin{bmatrix} 1 & 0 & \Gamma_{01} - \omega_{03}\xi_2 \\ 0 & 1 & \Gamma_{02} + \omega_{03}\xi_1 \\ 0 & 0 & 1 + \omega_{01}\xi_2 - \omega_{02}\xi_1 \end{bmatrix}_{\boldsymbol{E}_i \otimes \boldsymbol{e}_j} \quad \text{and} \quad \boldsymbol{F} = \begin{bmatrix} 1 & 0 & \Gamma_1 - \omega_3\xi_2 \\ 0 & 1 & \Gamma_2 + \omega_3\xi_1 \\ 0 & 0 & \Gamma_3 + 1 + \omega_1\xi_2 - \omega_2\xi_1 \end{bmatrix}_{\boldsymbol{t}_i \otimes \boldsymbol{e}_j}. \tag{9}$$

We can define the "initial length" $\lambda_0 = 1 + \omega_{01}\xi_2 - \omega_{02}\xi_1$, and the deformation gradient of the deformed configuration relative to the undeformed configuration $\boldsymbol{F}_e$ can be obtained by

$$\boldsymbol{F}_e = \boldsymbol{F}\boldsymbol{F}_0^{-1} = \begin{bmatrix} 1 & 0 & \dfrac{(\Gamma_1 - \Gamma_{01}) - (\omega_3 - \omega_{03})\xi_2}{\lambda_0} \\ 0 & 1 & \dfrac{(\Gamma_2 - \Gamma_{02}) + (\omega_3 - \omega_{03})\xi_1}{\lambda_0} \\ 0 & 0 & \dfrac{\Gamma_3 + 1 + \omega_1\xi_2 - \omega_2\xi_1}{\lambda_0} \end{bmatrix}_{\boldsymbol{t}_i \otimes \boldsymbol{E}_j}. \tag{10}$$

The "effective deformation gradient" $\boldsymbol{F}_e$ can also be expressed as

$$\boldsymbol{F}_e = \begin{bmatrix} 1 & 0 & \varepsilon_{31} \\ 0 & 1 & \varepsilon_{32} \\ 0 & 0 & \varepsilon_{33} + 1 \end{bmatrix}_{\boldsymbol{t}_i \otimes \boldsymbol{E}_j}, \tag{11}$$

where $\varepsilon_{31} = [(\Gamma_1 - \Gamma_{01}) - (\omega_3 - \omega_{03})\xi_2]/\lambda_0$, $\varepsilon_{32} = [(\Gamma_2 - \Gamma_{02}) + (\omega_3 - \omega_{03})\xi_1]/\lambda_0$, and $\varepsilon_{33} = (\Gamma_3 + 1 + \omega_1\xi_2 - \omega_2\xi_1)/\lambda_0 - 1$ are the infinitesimal strains.

2.2. Constitutive equations

In this subsection, we derive the expression of the resultant force and moment for the isotropic and homogeneous curved rods. The Green strain tensor of the material in the rod $C = \frac{1}{2}\left(F_e^T F_e - I\right)$ can be represented as

$$
C = \begin{bmatrix} 0 & 0 & \dfrac{\varepsilon_{31}}{2} \\ 0 & 0 & \dfrac{\varepsilon_{32}}{2} \\ \dfrac{\varepsilon_{31}}{2} & \dfrac{\varepsilon_{32}}{2} & \varepsilon_{33} + \dfrac{1}{2}\left(\varepsilon_{31}^2 + \varepsilon_{32}^2 + \varepsilon_{33}^2\right) \end{bmatrix}_{E_i \otimes E_j} \approx \begin{bmatrix} 0 & 0 & \dfrac{\varepsilon_{31}}{2} \\ 0 & 0 & \dfrac{\varepsilon_{32}}{2} \\ \dfrac{\varepsilon_{31}}{2} & \dfrac{\varepsilon_{32}}{2} & \varepsilon_{33} \end{bmatrix}_{E_i \otimes E_j} .
\tag{12}
$$

It should be noted that the Green strain tensor is only exact when Poisson's ratio $\nu = 0$, because the rigid cross-section assumption exactly holds under the condition $\nu = 0$. For more general situations, the expression of the Green strain tensor should be modified to hold the zero normal stresses between longitudinal fibers of rods, and the modified Green strain tensor can be given by

$$
C = \begin{bmatrix} -\nu\varepsilon_{33} & 0 & \dfrac{\varepsilon_{31}}{2} \\ 0 & -\nu\varepsilon_{33} & \dfrac{\varepsilon_{32}}{2} \\ \dfrac{\varepsilon_{31}}{2} & \dfrac{\varepsilon_{32}}{2} & \varepsilon_{33} \end{bmatrix}_{E_i \otimes E_j} .
\tag{13}
$$

For linear elastic materials, the second Piola-Kirchhoff stress T follows the relations:

$$
T_{ij} = D_{ijkl}C_{kl}, \quad D_{ijkl} = 2\mu\left(\delta_{ik}\delta_{jl} + \frac{\nu}{1-2\nu}\delta_{ij}\delta_{kl}\right),
\tag{14}
$$

where D_{ijkl} is the elastic coefficients, μ is the shear modulus, and δ_{ij} is the Kronecker delta. The second Piola-Kirchhoff stress can be written in a tensor form:

$$
T = \begin{bmatrix} 0 & 0 & \mu\varepsilon_{31} \\ 0 & 0 & \mu\varepsilon_{32} \\ \mu\varepsilon_{31} & \mu\varepsilon_{32} & E\varepsilon_{33} \end{bmatrix}_{E_i \otimes E_j} ,
\tag{15}
$$

where E is Young's modulus. It should be noted that the large deformation of the most HMS rods is generally achieved through the large rotation, rather than large strain. The strain in rods is usually small, therefore the linear elastic model is adopted for the HMS rods in this work. Considering a cross-section in the undeformed configuration A, the resultant force and moment over the cross-section n and m can be given by [47,55]

$$
n = \int\!\!\int_A F_e T E_3 d\xi_1 d\xi_2 = \int\!\!\int_A \begin{bmatrix} \mu\varepsilon_{31} + E\varepsilon_{31}\varepsilon_{33} \\ \mu\varepsilon_{32} + E\varepsilon_{32}\varepsilon_{33} \\ E\varepsilon_{33} + E\varepsilon_{33}^2 \end{bmatrix}_{t_i} d\xi_1 d\xi_2 \approx \int\!\!\int_A \begin{bmatrix} \mu\varepsilon_{31} \\ \mu\varepsilon_{32} \\ E\varepsilon_{33} \end{bmatrix}_{t_i} d\xi_1 d\xi_2,
$$

$$
m = \int\!\!\int_A (x - r) \times F_e T E_3 d\xi_1 d\xi_2 \approx \int\!\!\int_A \begin{bmatrix} \xi_1 \\ \xi_2 \\ 0 \end{bmatrix}_{t_i} \times \begin{bmatrix} \mu\varepsilon_{31} \\ \mu\varepsilon_{32} \\ E\varepsilon_{33} \end{bmatrix}_{t_i} d\xi_1 d\xi_2.
\tag{16}
$$

To obtain the relations between deformation and the resultant force and moment, it is essential to apply the Taylor expansion to the infinitesimal strains ε_{31}, ε_{32}, and ε_{33}:

$$
\begin{aligned}
\varepsilon_{31} &= [(\Gamma_1 - \Gamma_{01}) - (\omega_3 - \omega_{03})\xi_2](1 - \omega_{01}\xi_2 + \omega_{02}\xi_1) + o(\varepsilon^2), \\
\varepsilon_{32} &= [(\Gamma_2 - \Gamma_{02}) + (\omega_3 - \omega_{03})\xi_1](1 - \omega_{01}\xi_2 + \omega_{02}\xi_1) + o(\varepsilon^2), \\
\varepsilon_{33} &= [\Gamma_3 + (\omega_1 - \omega_{01})\xi_2 - (\omega_2 - \omega_{02})\xi_1](1 - \omega_{01}\xi_2 + \omega_{02}\xi_1) + o(\varepsilon^2),
\end{aligned}
\tag{17}
$$

where $\varepsilon \sim \Gamma \sim \omega\xi$ are the infinitesimal quantities. We define the "effective shear" $\Gamma_{e\eta} = \Gamma_\eta - \Gamma_{0\eta}$, "effective tension" $\Gamma_{e3} = \Gamma_3$, and "effective curvature" $\omega_{ei} = \omega_i - \omega_{0i}$. Substituting Eq. (17) into Eq. (16) leads to

$$\boldsymbol{n} = \begin{bmatrix} \Gamma_{e1}\mu A_1 + \omega_{e3}\omega_{01}\mu I_1 \\ \Gamma_{e2}\mu A_2 + \omega_{e3}\omega_{02}\mu I_2 \\ \Gamma_{e3}EA_s - \omega_{e1}\omega_{01}EI_1 - \omega_{e2}\omega_{02}EI_2 \end{bmatrix}_{t_i},$$

$$\boldsymbol{m} = \begin{bmatrix} \omega_{e1}EI_1 - \omega_{01}\Gamma_{e3}EI_1 - \omega_{e1}(\omega_{01}EI_{11} - \omega_{02}EI_{12}) + \omega_{e2}(\omega_{01}EI_{12} - \omega_{02}EI_{21}) \\ \omega_{e2}EI_2 - \omega_{02}\Gamma_{e3}EI_2 + \omega_{e2}(\omega_{02}EI_{22} - \omega_{01}EI_{21}) + \omega_{e1}(\omega_{01}EI_{12} - \omega_{02}EI_{21}) \\ \omega_{e3}\mu J + \Gamma_{e1}\omega_{01}\mu I_1 + \Gamma_{e2}\omega_{02}\mu I_2 + \omega_{e3}(\omega_{02}\mu I_{22} + \omega_{02}\mu I_{12} - \omega_{01}\mu I_{21} - \omega_{01}\mu I_{11}) \end{bmatrix}_{t_i},$$

(18)

where $A_\eta = k_\eta A_s$ is the equivalent shear area, and k_η is the reasonable factor [62]; A_s is the area of the cross-section; $I_1 = \int\int_A \xi_2^2 d\xi_1 d\xi_2$ and $I_2 = \int\int_A \xi_1^2 d\xi_1 d\xi_2$ are the moments of inertia of the cross-section; $J = I_1 + I_2$ is the polar moment of inertia of the cross-section; $I_{11} = \int\int_A \xi_2^3 d\xi_1 d\xi_2$, $I_{12} = \int\int_A \xi_1\xi_2^2 d\xi_1 d\xi_2$, $I_{21} = \int\int_A \xi_1^2\xi_2 d\xi_1 d\xi_2$ and $I_{22} = \int\int_A \xi_1^3 d\xi_1 d\xi_2$ are the high order moments of inertia of the cross-section. For standard symmetric solid cross-section shapes, the high-order moments of inertia of the cross-section $I_{11} = I_{12} = I_{21} = I_{22} = 0$, the resultant force $\boldsymbol{n}$ and the moment $\boldsymbol{m}$ can be expressed as

$$\boldsymbol{n} = \begin{bmatrix} \Gamma_{e1}\mu A_1 + \omega_{e3}\omega_{01}\mu I_1 \\ \Gamma_{e2}\mu A_2 + \omega_{e3}\omega_{02}\mu I_2 \\ \Gamma_{e3}EA_s - \omega_{e1}\omega_{01}EI_1 - \omega_{e2}\omega_{02}EI_2 \end{bmatrix}_{t_i},$$

$$\boldsymbol{m} = \begin{bmatrix} \omega_{e1}EI_1 - \omega_{01}\Gamma_{e3}EI_1 \\ \omega_{e2}EI_2 - \omega_{02}\Gamma_{e3}EI_2 \\ \omega_{e3}\mu J + \Gamma_{e1}\omega_{01}\mu I_1 + \Gamma_{e2}\omega_{02}\mu I_2 \end{bmatrix}_{t_i}.$$

(19)

Eq. (19) indicates the two coupling effects: (1) "tension-bending" coupling effects: the coupling of the tension deformation Γ_{e3} and the bending deformation $\omega_{e\eta}$ determines the tension resultant forces and bending moment; (2) "shear-torsion" coupling effects: the coupling of the shear deformation $\Gamma_{e\eta}$ and the torsional deformation ω_{e3} determines the shear resultant forces and torsion moment. The material resultant force and moment $\boldsymbol{N}$ and $\boldsymbol{M}$, material effective strain measures $\boldsymbol{\Gamma}_e$ and $\boldsymbol{\omega}_e$ can be defined as

$$\boldsymbol{N} = \Lambda_r^T \boldsymbol{n}, \quad \boldsymbol{M} = \Lambda_r^T \boldsymbol{m},$$
$$\boldsymbol{\Gamma}_e = \Gamma_{e1}\boldsymbol{E}_1 + \Gamma_{e2}\boldsymbol{E}_2 + \Gamma_{e3}\boldsymbol{E}_3,$$
$$\boldsymbol{\omega}_e = \omega_{e1}\boldsymbol{E}_1 + \omega_{e2}\boldsymbol{E}_2 + \omega_{e3}\boldsymbol{E}_3,$$

(20)

where the material effective strain measures have other expressions as $\boldsymbol{\Gamma}_e = \Lambda_r^T \frac{\partial \boldsymbol{r}}{\partial S} - \frac{\partial \boldsymbol{r}_0}{\partial S}$ and $\boldsymbol{\omega}_e^\wedge = \Lambda_r^T \frac{\partial \Lambda_r}{\partial S}$. Finally, the material elasticity tensor can be obtained as

$$\boldsymbol{D} = \begin{bmatrix} \dfrac{\partial \boldsymbol{N}}{\partial \boldsymbol{\Gamma}_e} & \dfrac{\partial \boldsymbol{N}}{\partial \boldsymbol{\omega}_e} \\ \dfrac{\partial \boldsymbol{M}}{\partial \boldsymbol{\Gamma}_e} & \dfrac{\partial \boldsymbol{M}}{\partial \boldsymbol{\omega}_e} \end{bmatrix} = \begin{bmatrix} \mu A_1 & 0 & 0 & 0 & 0 & \omega_{01}\mu I_1 \\ 0 & \mu A_2 & 0 & 0 & 0 & \omega_{02}\mu I_2 \\ 0 & 0 & EA_s & -\omega_{01}EI_1 & -\omega_{02}EI_2 & 0 \\ 0 & 0 & -\omega_{01}EI_1 & EI_1 & 0 & 0 \\ 0 & 0 & -\omega_{02}EI_2 & 0 & EI_2 & 0 \\ \omega_{01}\mu I_1 & \omega_{02}\mu I_2 & 0 & 0 & 0 & \mu J \end{bmatrix}_{\boldsymbol{E}_i \otimes \boldsymbol{E}_j}.$$

(21)

Hereto the constitutive equations with the centroids as the reference points are completed. However, for dynamic analysis, the relative coordinates of the mass of centers ξ_1^c and ξ_2^c are important, and can be obtained by

$$\xi_1^c = \frac{\int\int_A \rho\xi_1\lambda_0 d\xi_1 d\xi_2}{\int\int_A \rho\lambda_0 d\xi_1 d\xi_2} = -\frac{\omega_{02}I_2}{A_s},$$

$$\xi_2^c = \frac{\int\int_A \rho\xi_2\lambda_0 d\xi_1 d\xi_2}{\int\int_A \rho\lambda_0 d\xi_1 d\xi_2} = \frac{\omega_{01}I_1}{A_s},$$

(22)

where ρ is the mass density. The spatial relative vector $\boldsymbol{\xi}^c = \xi_1^c \boldsymbol{t}_1 + \xi_2^c \boldsymbol{t}_2$ and material relative vector $\boldsymbol{\xi}_0^c = \xi_1^c \boldsymbol{E}_1 + \xi_2^c \boldsymbol{E}_2$ can be defined.

2.3. Reduced balance equations

In this subsection, the reduced balance equations of the HMS curved rods are summarized. Prior to introducing the linear and angular momentum of the curved rods, the time derivatives of the moving frame should be defined, and it can be given by

$$\frac{\partial \boldsymbol{t}_i}{\partial \tau} = \boldsymbol{w} \times \boldsymbol{t}_i = (w_1\boldsymbol{t}_1 + w_2\boldsymbol{t}_2 + w_3\boldsymbol{t}_3) \times \boldsymbol{t}_i, \quad \boldsymbol{w}^\wedge = \frac{\partial \Lambda_r}{\partial \tau}\Lambda_r^T,$$

(23)

where $\boldsymbol{w}$ is the angular velocity of the cross-sections. For convenience, we denote material time derivative by a superposed "dot". Considering an arbitrary cross-section, the linear momentum per unit of reference arc length $\boldsymbol{L}_t$ can be defined by

$$\boldsymbol{L}_t = \int\int_A \rho\lambda_0\dot{\boldsymbol{x}}d\xi_1 d\xi_2 = \rho A_s(\dot{\boldsymbol{r}} + \boldsymbol{w}\times\boldsymbol{\xi}^c). \tag{24}$$

Similarly, the angular momentum per unit of reference arc length $\boldsymbol{H}_t$ referred to the centroids can be given by

$$
\begin{aligned}
\boldsymbol{H}_t &= \int\int_A \rho\lambda_0(\boldsymbol{x}-\boldsymbol{r})\times(\dot{\boldsymbol{x}}-\dot{\boldsymbol{r}})d\xi_1 d\xi_2 \\
&= \int\int_A \rho\lambda_0(\boldsymbol{x}-\boldsymbol{r})\times[\boldsymbol{w}\times(\boldsymbol{x}-\boldsymbol{r})]d\xi_1 d\xi_2 \\
&= \int\int_A \rho\lambda_0\big[\|\boldsymbol{x}-\boldsymbol{r}\|^2\boldsymbol{1}-(\boldsymbol{x}-\boldsymbol{r})\otimes(\boldsymbol{x}-\boldsymbol{r})\big]d\xi_1 d\xi_2\boldsymbol{w} = \boldsymbol{I}_\rho\boldsymbol{w},
\end{aligned}
\tag{25}
$$

where $\boldsymbol{I}_\rho$ is the inertia tensor referred to as the centroids, and for the standard symmetric solid cross-section shapes, it can be expressed as

$$\boldsymbol{I}_\rho = \begin{bmatrix} \rho I_1 & 0 & 0 \\ 0 & \rho I_2 & 0 \\ 0 & 0 & \rho J \end{bmatrix}_{\boldsymbol{t}_i\otimes\boldsymbol{t}_j}. \tag{26}$$

The reduced balance equations of the curved rod are, see e.g., Simo [47] or Kapania [55],

$$
\begin{aligned}
\frac{\partial\boldsymbol{n}}{\partial S} + \overline{\boldsymbol{n}} &= \dot{\boldsymbol{L}}_t = \rho A_s[\ddot{\boldsymbol{r}} + \dot{\boldsymbol{w}}\times\boldsymbol{\xi}^c + \boldsymbol{w}\times(\boldsymbol{w}\times\boldsymbol{\xi}^c)], \\
\frac{\partial\boldsymbol{m}}{\partial S} + \frac{\partial\boldsymbol{r}}{\partial S}\times\boldsymbol{n} + \overline{\boldsymbol{m}} &= \dot{\boldsymbol{H}}_t + \rho A_s\boldsymbol{\xi}^c\times\ddot{\boldsymbol{r}} = \boldsymbol{I}_\rho\dot{\boldsymbol{w}} + \boldsymbol{w}\times\boldsymbol{I}_\rho\boldsymbol{w} + \rho A_s\boldsymbol{\xi}^c\times\ddot{\boldsymbol{r}},
\end{aligned}
\tag{27}
$$

where $\overline{\boldsymbol{n}}$ and $\overline{\boldsymbol{m}}$ is the "applied" distributed load. In application, it is convenient to utilize the material form of the equations. Thus, we can define the material vector fields:

$$
\begin{aligned}
\boldsymbol{W} &= \boldsymbol{\Lambda}_r^T\boldsymbol{w} = w_1\boldsymbol{E}_1 + w_2\boldsymbol{E}_2 + w_3\boldsymbol{E}_3, \\
\overline{\boldsymbol{N}} &= \boldsymbol{\Lambda}_r^T\overline{\boldsymbol{n}}, \quad \overline{\boldsymbol{M}} = \boldsymbol{\Lambda}_r^T\overline{\boldsymbol{m}}, \\
\boldsymbol{J}_\rho &= \boldsymbol{\Lambda}_r^T\boldsymbol{I}_\rho\boldsymbol{\Lambda}_r = = \begin{bmatrix} \rho I_1 & 0 & 0 \\ 0 & \rho I_2 & 0 \\ 0 & 0 & \rho J \end{bmatrix}_{\boldsymbol{E}_i\otimes\boldsymbol{E}_j}.
\end{aligned}
\tag{28}
$$

For HMS curved rods, such as hard-magnetic soft robotics, the applied load can be divided into three parts: gravity loads $\overline{\boldsymbol{n}}_g$ and $\overline{\boldsymbol{m}}_g$, magnetic driving forces $\overline{\boldsymbol{n}}_m$ and $\overline{\boldsymbol{m}}_m$, and other applied loads $\overline{\boldsymbol{n}}_o$ and $\overline{\boldsymbol{m}}_o$. To simplify the discussion, the loads $\overline{\boldsymbol{n}}_m$ and $\overline{\boldsymbol{m}}_m$ are assumed to be invariant under the deformation of the HMS curved rod. Therefore, we focus our attention on the first two kinds of loads. The gravity loads can be expressed as

$$
\begin{aligned}
\overline{\boldsymbol{n}}_g &= \int\int_A \rho\lambda_0\boldsymbol{g}d\xi_1 d\xi_2 = \rho A_s\boldsymbol{g}, \\
\overline{\boldsymbol{m}}_g &= \int\int_A \rho\lambda_0(\boldsymbol{x}-\boldsymbol{r})\times\boldsymbol{g}d\xi_1 d\xi_2 = \rho A_s\boldsymbol{\xi}^c\times\boldsymbol{g},
\end{aligned}
\tag{29}
$$

where $\boldsymbol{g}$ is the gravitational acceleration. For straight rods, the geometry centroids and the centers of mass coincide, which means the moment $\overline{\boldsymbol{m}}_g$ caused by gravity is zero.

In this work, the HMS materials are assumed to be ideal HMS materials, and their magnetic free energy density under gradient-invariant applied magnetic field can be expressed as [30]

$$
\begin{aligned}
\rho_m &= -\frac{1}{\mu_m}\boldsymbol{B}_a\cdot\boldsymbol{\Lambda}_r\boldsymbol{B}_r \\
&= -\frac{1}{\mu_m}[\boldsymbol{B}_0 + (\nabla\boldsymbol{B}_0)(\boldsymbol{x}-\boldsymbol{r})]\cdot\boldsymbol{\Lambda}_r\boldsymbol{B}_r,
\end{aligned}
\tag{30}
$$

where ρ_m is the magnetic free energy density, μ_m is the vacuum permeability, $\boldsymbol{B}_a$ is the applied magnetic flux density, $\boldsymbol{B}_r$ is the residual magnetic flux density in the undeformed configuration, $\boldsymbol{B}_0$ is the applied magnetic flux density in the centroids, and $\nabla\boldsymbol{B}_0$ is the gradient of the applied magnetic flux density. For ideal HMS materials, we assume the $\boldsymbol{B}_a$ and $\boldsymbol{B}_r$ are known and unaltered, as a simplification. The distribution of the magnetic fields will be affected by the magnetic dipole moments of the hard-magnetic particles and the fringing effects on the HMS materials. The magnetic free energy per unit of the reference arc length U_m can be given by

$$U_m = \int \int_A \lambda_0 \rho_m d\xi_1 d\xi_2$$

$$= -\frac{A_s}{\mu_m}[\boldsymbol{B}_0 + (\nabla \boldsymbol{B}_0)\boldsymbol{\xi}^c] \cdot \boldsymbol{\Lambda}_r \boldsymbol{B}_r \tag{31}$$

To obtain the magnetic driving forces, we consider an arbitrary configuration of the rods $\widetilde{\boldsymbol{\Phi}} = \{\widetilde{\boldsymbol{r}}, \widetilde{\boldsymbol{\Lambda}}_r\}$ and an infinitesimal perturbation $\delta\boldsymbol{\Phi} = \{\delta\boldsymbol{r}, \delta\boldsymbol{\theta}\}$. It is obvious that we can express the perturbated configuration $\overline{\boldsymbol{\Phi}} = \{\overline{\boldsymbol{r}}, \overline{\boldsymbol{\Lambda}}_r\}$ as

$$\overline{\boldsymbol{r}} = \widetilde{\boldsymbol{r}} + \delta\boldsymbol{r},$$
$$\overline{\boldsymbol{\Lambda}}_r = \exp(\delta\boldsymbol{\theta}^\wedge)\widetilde{\boldsymbol{\Lambda}}_r = \widetilde{\boldsymbol{\Lambda}}_r + \delta\boldsymbol{\theta}^\wedge \widetilde{\boldsymbol{\Lambda}}_r. \tag{32}$$

In this work, a variable with a tilde or a bar above it represents the variable in the configuration $\widetilde{\boldsymbol{\Phi}}$ or $\overline{\boldsymbol{\Phi}}$, respectively. The variation of the magnetic free energy per unit of the reference arc length δU_m can be given by

$$\delta U_m = \overline{U}_m - \widetilde{U}_m = -\left(\delta\boldsymbol{r}^T \widetilde{\overline{\boldsymbol{n}}}_m + \delta\boldsymbol{\theta}^T \widetilde{\overline{\boldsymbol{m}}}_m\right)$$

$$= -\frac{A_s}{\mu_m}\begin{bmatrix} \delta\boldsymbol{r}^T & \delta\boldsymbol{\theta}^T \end{bmatrix}\begin{bmatrix} (\nabla\widetilde{\boldsymbol{B}}_0)^T \widetilde{\boldsymbol{\Lambda}}_r \widetilde{\boldsymbol{B}}_r \\ \widetilde{\boldsymbol{\Lambda}}_r \widetilde{\boldsymbol{B}}_r \times (\widetilde{\boldsymbol{B}}_0 + \nabla\widetilde{\boldsymbol{B}}_0 \widetilde{\boldsymbol{\xi}}^c) + \widetilde{\boldsymbol{\xi}}^c \times (\nabla\widetilde{\boldsymbol{B}}_0)^T \widetilde{\boldsymbol{\Lambda}}_r \widetilde{\boldsymbol{B}}_r \end{bmatrix}. \tag{33}$$

Therefore, the magnetic driving forces $\overline{\boldsymbol{n}}_m$ and $\overline{\boldsymbol{m}}_m$ can be expressed as

$$\overline{\boldsymbol{n}}_m = \frac{A_s}{\mu_m}(\nabla\boldsymbol{B}_0)^T \boldsymbol{\Lambda}_r \boldsymbol{B}_r,$$

$$\overline{\boldsymbol{m}}_m = \frac{A_s}{\mu_m}\left[\boldsymbol{\Lambda}_r \boldsymbol{B}_r \times (\boldsymbol{B}_0 + \nabla\boldsymbol{B}_0 \boldsymbol{\xi}^c) + \boldsymbol{\xi}^c \times (\nabla\boldsymbol{B}_0)^T \boldsymbol{\Lambda}_r \boldsymbol{B}_r\right] \approx \frac{A_s}{\mu_m}\boldsymbol{\Lambda}_r \boldsymbol{B}_r \times \boldsymbol{B}_0. \tag{34}$$

Because the condition $\|\boldsymbol{B}_0\| \gg \|\nabla\boldsymbol{B}_0\boldsymbol{\xi}^c\|$ is appropriate for most hard-magnetic soft robotics, the second and third terms of the moment caused by magnetic fields are ignored.

Here, we may summarize the governing equations of hard-magnetic soft robotics as follows:

$$\frac{\partial\boldsymbol{n}}{\partial S} + \overline{\boldsymbol{n}}_g + \overline{\boldsymbol{n}}_m + \overline{\boldsymbol{n}}_o = \rho A_s[\ddot{\boldsymbol{r}} + \dot{\boldsymbol{w}} \times \boldsymbol{\xi}^c + \boldsymbol{w} \times (\boldsymbol{w} \times \boldsymbol{\xi}^c)],$$

$$\frac{\partial\boldsymbol{m}}{\partial S} + \frac{\partial\boldsymbol{r}}{\partial S} \times \boldsymbol{n} + \overline{\boldsymbol{m}}_g + \overline{\boldsymbol{m}}_m + \overline{\boldsymbol{m}}_o = \boldsymbol{I}_\rho\dot{\boldsymbol{w}} + \boldsymbol{w} \times \boldsymbol{I}_\rho\boldsymbol{w} + \rho A_s\boldsymbol{\xi}^c \times \ddot{\boldsymbol{r}},$$

$$\overline{\boldsymbol{n}}_g = \rho A_s\boldsymbol{g}, \quad \overline{\boldsymbol{m}}_g = \rho A_s\boldsymbol{\xi}^c \times \boldsymbol{g},$$

$$\overline{\boldsymbol{n}}_m = \frac{A_s}{\mu_m}(\nabla\boldsymbol{B}_0)^T \boldsymbol{\Lambda}_r \boldsymbol{B}_r, \quad \overline{\boldsymbol{m}}_m \approx \frac{A_s}{\mu_m}\boldsymbol{\Lambda}_r \boldsymbol{B}_r \times \boldsymbol{B}_0. \tag{35}$$

3. Finite element formulation

In this section, we start by presenting the weak form of the problem, followed by the temporal discretization and the linearization of the weak form. In the end, we complete the finite element formulation of the problem by spatial discretization using Lagrange interpolation polynomials.

3.1. Weak form of the reduced balanced equations

For simplicity, the boundary conditions are assumed to be Dirichlet type, and the weak form of the reduced balanced equations of the HMS curved rod can be given by

$$G(\Phi, \delta\Phi) = -\int_0^L \left[\delta\boldsymbol{r}^T\frac{\partial\boldsymbol{n}}{\partial S} + \delta\boldsymbol{\theta}^T\left(\frac{\partial\boldsymbol{m}}{\partial S} + \frac{\partial\boldsymbol{r}}{\partial S} \times \boldsymbol{n}\right)\right]dS$$

$$-\int_0^L \left[\delta\boldsymbol{r}^T\left(\overline{\boldsymbol{n}}_g + \overline{\boldsymbol{n}}_m + \overline{\boldsymbol{n}}_o\right) + \delta\boldsymbol{\theta}^T\left(\overline{\boldsymbol{m}}_g + \overline{\boldsymbol{m}}_m + \overline{\boldsymbol{m}}_o\right)\right]dS \tag{36}$$

$$+\int_0^L \left\{\delta\boldsymbol{r}^T\rho A_s[\ddot{\boldsymbol{r}} + \dot{\boldsymbol{w}} \times \boldsymbol{\xi}^c + \boldsymbol{w} \times (\boldsymbol{w} \times \boldsymbol{\xi}^c)] + \delta\boldsymbol{\theta}^T(\boldsymbol{I}_\rho\dot{\boldsymbol{w}} + \boldsymbol{w} \times \boldsymbol{I}_\rho\boldsymbol{w} + \rho A_s\boldsymbol{\xi}^c \times \ddot{\boldsymbol{r}})\right\}dS = 0.$$

The weak form can be divided into three parts: the part caused by resultant force and moment G_r, the part caused by the applied distributed load G_a, and the part caused by the dynamical part G_d. Their expressions are

$$G_r = -\int_0^L \left[\delta \boldsymbol{r}^T \frac{\partial \boldsymbol{n}}{\partial S} + \delta \boldsymbol{\theta}^T \left(\frac{\partial \boldsymbol{m}}{\partial S} + \frac{\partial \boldsymbol{r}}{\partial S} \times \boldsymbol{n} \right) \right] dS,$$

$$G_a = -\int_0^L \left[\delta \boldsymbol{r}^T (\overline{\boldsymbol{n}}_g + \overline{\boldsymbol{n}}_m + \overline{\boldsymbol{n}}_o) + \delta \boldsymbol{\theta}^T (\overline{\boldsymbol{m}}_g + \overline{\boldsymbol{m}}_m + \overline{\boldsymbol{m}}_o) \right] dS, \tag{37}$$

$$G_d = \int_0^L \left\{ \delta \boldsymbol{r}^T \rho A_s [\ddot{\boldsymbol{r}} + \dot{\boldsymbol{w}} \times \boldsymbol{\xi}^c + \boldsymbol{w} \times (\boldsymbol{w} \times \boldsymbol{\xi}^c)] + \delta \boldsymbol{\theta}^T (I_\rho \dot{\boldsymbol{w}} + \boldsymbol{w} \times I_\rho \boldsymbol{w} + \rho A_s \boldsymbol{\xi}^c \times \ddot{\boldsymbol{r}}) \right\} dS.$$

For Dirichlet boundary conditions, the condition $\delta \boldsymbol{r}(0) = \delta \boldsymbol{r}(L) = \delta \boldsymbol{\theta}(0) = \delta \boldsymbol{\theta}(L) = 0$ holds, and integration-by-part of G_r leads to

$$G_r = \int_0^L \left\{ \left[\frac{\partial (\delta \boldsymbol{r})}{\partial S} - \delta \boldsymbol{\theta} \times \frac{\partial \boldsymbol{r}}{\partial S} \right]^T \boldsymbol{n} + \frac{\partial (\delta \boldsymbol{\theta})^T}{\partial S} \boldsymbol{m} \right\} dS. \tag{38}$$

It is sometimes convenient to consider the material description of the weak form. The G_r in the material description can be expressed as

$$G_r = \int_0^L \left\{ \left[\frac{\partial (\delta \boldsymbol{r})}{\partial S} - \delta \boldsymbol{\theta} \times \frac{\partial \boldsymbol{r}}{\partial S} \right]^T \boldsymbol{\Lambda}_r \boldsymbol{N} + \frac{\partial (\delta \boldsymbol{\theta})^T}{\partial S} \boldsymbol{\Lambda}_r \boldsymbol{M} \right\} dS. \tag{39}$$

The G_d in the material description can be expressed as

$$\begin{aligned} G_d = &\int_0^L \left[\delta \boldsymbol{r}^T \rho A_s \ddot{\boldsymbol{r}} + \delta \boldsymbol{\theta}^T (\rho A_s \boldsymbol{\xi}^c \times \ddot{\boldsymbol{r}}) \right] dS \\ &+ \int_0^L \left\{ \delta \boldsymbol{r}^T \rho A_s \boldsymbol{\Lambda}_r \left[\dot{\boldsymbol{W}} \times \boldsymbol{\xi}_0^c + \boldsymbol{W} \times (\boldsymbol{W} \times \boldsymbol{\xi}_0^c) \right] + \delta \boldsymbol{\theta}^T \boldsymbol{\Lambda}_r (\boldsymbol{J}_\rho \dot{\boldsymbol{W}} + \boldsymbol{W} \times \boldsymbol{J}_\rho \boldsymbol{W}) \right\} dS, \end{aligned} \tag{40}$$

where $\dot{\boldsymbol{W}} = \boldsymbol{\Lambda}_r^T \dot{\boldsymbol{w}}$ is the angular acceleration in the material description.

3.2. Temporal discretization

Let $[\tau_n, \tau_{n+1}] \subset [0, T]$ denotes a typical time sub-interval, and we employ the subscript n to denote the approximation of the quantity at the time instance τ_n. The state of the rod at the time τ_n can be described by its configuration $\Phi_n = \{\boldsymbol{r}_n, \boldsymbol{\Lambda}_{r(n)}\}$, its linear and angular velocities $\{\dot{\boldsymbol{r}}_n, \boldsymbol{w}_n\}$, and its linear and angular acceleration $\{\ddot{\boldsymbol{r}}_n, \dot{\boldsymbol{w}}_n\}$. The displacement field of the rod from τ_n to τ_{n+1} can be defined as $\{\boldsymbol{u}_n, \boldsymbol{\theta}_n\}$, and the relation between Φ_n and Φ_{n+1} can be given by

$$\begin{aligned} \boldsymbol{r}_{n+1} &= \boldsymbol{r}_n + \boldsymbol{u}_n, \\ \boldsymbol{\Lambda}_{r(n+1)} &= \exp(\boldsymbol{\theta}_n^\wedge) \boldsymbol{\Lambda}_{r(n)} = \boldsymbol{\Lambda}_{r(n)} \exp(\boldsymbol{\Theta}_n^\wedge), \end{aligned} \tag{41}$$

where $\boldsymbol{\Theta}_n = \boldsymbol{\Lambda}_{r(n)}^T \boldsymbol{\theta}_n$ is the rotation displacement in the material description. We adopt the Newmark method for numerical time integration. The updated quantity of translational motion can be given by

$$\begin{aligned} \boldsymbol{u}_n &= h \dot{\boldsymbol{r}}_n + h^2 \left[\left(\frac{1}{2} - \beta \right) \ddot{\boldsymbol{r}}_n + \beta \ddot{\boldsymbol{r}}_{n+1} \right], \\ \dot{\boldsymbol{r}}_{n+1} &= \dot{\boldsymbol{r}}_n + h[(1 - \gamma) \ddot{\boldsymbol{r}}_n + \gamma \ddot{\boldsymbol{r}}_{n+1}], \end{aligned} \tag{42}$$

where $h = \tau_{n+1} - \tau_n$ is the time step size, $\beta \in \left[0, \frac{1}{2} \right]$ and $\gamma \in [0, 1]$ are the parameters for the Newmark scheme. The updated quantity in the material description of rotational motion can be given by

$$\begin{aligned} \boldsymbol{\Theta}_n &= h \boldsymbol{W}_n + h^2 \left[\left(\frac{1}{2} - \beta \right) \dot{\boldsymbol{W}}_n + \beta \dot{\boldsymbol{W}}_{n+1} \right], \\ \boldsymbol{W}_{n+1} &= \boldsymbol{W}_n + h[(1 - \gamma) \dot{\boldsymbol{W}}_n + \gamma \dot{\boldsymbol{W}}_{n+1}]. \end{aligned} \tag{43}$$

For nonlinear dynamic analysis, the consistent Newton-Raphson method is adopted. The quantity $(\bullet)$ in the ith iteration at the time τ_{n+1} is denoted by $(\bullet)_{n+1}^{(i)}$. For $i = 0$, the initial quantity can be set as $\left\{ \boldsymbol{u}_n^{(0)}, \boldsymbol{\Theta}_{n+1}^{(0)} \right\} = \{\boldsymbol{0}, \boldsymbol{0}\}$, and the other quantities are updated according to Eqs. (41), (42) and (43). Considering the ith ($i \neq 0$) iteration, the iterative displacement increment field $\Delta \Phi_{n+1}^{(i)} = \left\{ \Delta \boldsymbol{r}_{n+1}^{(i)}, \Delta \boldsymbol{\vartheta}_{n+1}^{(i)} \right\}$ can be obtained by solving the linearization of the weak form. The updated quantity of the translational motion in the $i + 1$-th iteration can be given by

$$\boldsymbol{r}_{n+1}^{(i+1)} = \boldsymbol{r}_{n+1}^{(i)} + \Delta \boldsymbol{r}_{n+1}^{(i)},$$

$$\dot{\boldsymbol{r}}_{n+1}^{(i+1)} = \dot{\boldsymbol{r}}_{n+1}^{(i)} + \frac{\gamma}{\beta h} \Delta \boldsymbol{r}_{n+1}^{(i)},$$

$$\ddot{\boldsymbol{r}}_{n+1}^{(i+1)} = \ddot{\boldsymbol{r}}_{n+1}^{(i)} + \frac{1}{\beta h^2} \Delta \boldsymbol{r}_{n+1}^{(i)}. \tag{44}$$

The updated quantity of the rotational motion in the $i + 1$-th iteration can be given by

$$\boldsymbol{\Lambda}_{r(n+1)}^{(i+1)} = \exp\left[\Delta \boldsymbol{\vartheta}_{n+1}^{(i)\wedge}\right] \boldsymbol{\Lambda}_{r(n+1)}^{(i)},$$

$$\boldsymbol{\theta}_n^{(i+1)\wedge} = \ln\left\{\exp\left[\Delta \boldsymbol{\vartheta}_{n+1}^{(i)\wedge}\right] \exp\left[\boldsymbol{\theta}_n^{(i)\wedge}\right]\right\},$$

$$\boldsymbol{\Theta}_n^{(i+1)} = \boldsymbol{\Lambda}_{r(n)}^T \boldsymbol{\theta}_n^{(i+1)},$$

$$\boldsymbol{W}_{n+1}^{(i+1)} = \boldsymbol{W}_{n+1}^{(i)} + \frac{\gamma}{\beta h}\left[\boldsymbol{\Theta}_n^{(i+1)} - \boldsymbol{\Theta}_n^{(i)}\right],$$

$$\dot{\boldsymbol{W}}_{n+1}^{(i+1)} = \dot{\boldsymbol{W}}_{n+1}^{(i)} + \frac{1}{\beta h^2}\left[\boldsymbol{\Theta}_n^{(i+1)} - \boldsymbol{\Theta}_n^{(i)}\right]. \tag{45}$$

The detailed scheme to calculate the $\ln\left\{\exp\left[\Delta \boldsymbol{\vartheta}_{n+1}^{(i)\wedge}\right] \exp\left[\boldsymbol{\theta}_n^{(i)\wedge}\right]\right\}$ can be found in Appendix B of [63].

3.3. Linearization of the weak form

Considering the ith iteration at the time τ_{n+1}, the iterative displacement increment field is denoted by $\Delta \Phi_{n+1}^{(i)} = \left\{\Delta \boldsymbol{r}_{n+1}^{(i)}, \Delta \boldsymbol{\vartheta}_{n+1}^{(i)}\right\}$. From Eq. (44), the linear part of the change of the translational quantity $\left\{\delta \boldsymbol{r}_{n+1}^{(i)}, \delta \dot{\boldsymbol{r}}_{n+1}^{(i)}, \delta \ddot{\boldsymbol{r}}_{n+1}^{(i)}\right\}$ can be given by

$$\delta \boldsymbol{r}_{n+1}^{(i)} = \Delta \boldsymbol{r}_{n+1}^{(i)},$$

$$\delta \dot{\boldsymbol{r}}_{n+1}^{(i)} = \frac{\gamma}{\beta h} \Delta \boldsymbol{r}_{n+1}^{(i)},$$

$$\delta \ddot{\boldsymbol{r}}_{n+1}^{(i)} = \frac{1}{\beta h^2} \Delta \boldsymbol{r}_{n+1}^{(i)}. \tag{46}$$

For rotational quantity, the key step is to determine the linear part of the change of the rotational displacement field $\delta \boldsymbol{\theta}_n^i$, and it can be obtained by [63]

$$\delta \boldsymbol{\theta}_n^i = \frac{d}{d\varepsilon}\bigg|_{\varepsilon=0} \ln\left\{\exp\left[\varepsilon \Delta \boldsymbol{\vartheta}_{n+1}^{(i)\wedge}\right] \exp\left[\boldsymbol{\theta}_n^{(i)}\right]\right\}^{\vee} = \boldsymbol{Z}\left(\boldsymbol{\theta}_n^{(i)}\right) \Delta \boldsymbol{\vartheta}_{n+1}^{(i)},$$

$$\boldsymbol{Z}(\boldsymbol{\theta}) = \boldsymbol{e} \otimes \boldsymbol{e} + \frac{\| \boldsymbol{\theta} \| / 2}{\tan(\| \boldsymbol{\theta} \| / 2)}(\boldsymbol{1} - \boldsymbol{e} \otimes \boldsymbol{e}) - \frac{\boldsymbol{\theta}^{\wedge}}{2}, \quad \text{where} \quad \boldsymbol{e} = \boldsymbol{\theta} / \| \boldsymbol{\theta} \|. \tag{47}$$

Therefore, according to Eqs. (45) and (47), the linear part of the change of other rotational quantity $\left\{\delta \boldsymbol{\Lambda}_{r(n+1)}^{(i)}, \delta \boldsymbol{W}_{n+1}^{(i)}, \delta \dot{\boldsymbol{W}}_{n+1}^{(i)}\right\}$ can be obtained by

$$\delta \boldsymbol{\Lambda}_{r(n+1)}^{(i)} = \left[\Delta \boldsymbol{\vartheta}_{n+1}^{(i)}\right]^{\wedge} \boldsymbol{\Lambda}_{r(n+1)}^{(i)},$$

$$\delta \boldsymbol{W}_{n+1}^{(i)} = \frac{\gamma}{\beta h} \boldsymbol{\Lambda}_{r(n)}^T \boldsymbol{Z}\left(\boldsymbol{\theta}_n^{(i)}\right) \Delta \boldsymbol{\vartheta}_{n+1}^{(i)},$$

$$\delta \dot{\boldsymbol{W}}_{n+1}^{(i)} = \frac{1}{\beta h^2} \boldsymbol{\Lambda}_{r(n)}^T \boldsymbol{Z}\left(\boldsymbol{\theta}_n^{(i)}\right) \Delta \boldsymbol{\vartheta}_{n+1}^{(i)}. \tag{48}$$

Considering the linearization of the weak form in the ith iteration at the time τ_{n+1} about the configuration $\Phi_{n+1}^{(i)}$, and it can be defined as

$$L\left\{G\left[\Phi_{n+1}^{(i)}, \delta\Phi\right]\right\} = G\left[\Phi_{n+1}^{(i)}, \delta\Phi\right] + \delta G_r + \delta G_a + \delta G_d = 0, \tag{49}$$

where $G\left[\Phi_{n+1}^{(i)}, \delta\Phi\right]$ is the out-of-balance dynamic force, δG_r, δG_a and δG_d are the linear part of the change of the weak form. For convenience, we can define the test functions $\delta\Phi$ and the trial functions $\Delta\Phi$ as the form as

$$\delta\boldsymbol{\Phi} = \begin{bmatrix} \delta \boldsymbol{r} \\ \delta \boldsymbol{\theta} \end{bmatrix}, \quad \Delta\boldsymbol{\Phi} = \begin{bmatrix} \Delta \boldsymbol{r} \\ \Delta \boldsymbol{\vartheta} \end{bmatrix}. \tag{50}$$

Following the definition in Section 2.3, a variable with a tilde above it represents the variable in the current configuration $\Phi^{(i)}_{n+1}$, e. g., $\Lambda^{(i)}_{r(n+1)} = \widetilde{\Lambda}_r$.

The linear part caused by the resultant force and moment δG_r in Eq. (49) can be given by

$$\delta G_r\left[\Phi^{(i)}_{n+1}, \delta\Phi\right] = \int_0^L \left[\left(\widetilde{\Xi}^T\delta\Phi\right)^T\widetilde{d}\,\widetilde{\Xi}^T + \left(\widetilde{\Psi}^T\delta\Phi\right)^T\widetilde{Y}\widetilde{\Psi}^T\right]\Delta\Phi^{(i)}_{n+1}dS, \tag{51}$$

where d is the spatial form of the material elasticity tensor and take the following form

$$d = \Pi D \Pi^T, \quad \Pi = \begin{bmatrix} \Lambda_r & 0 \\ 0 & \Lambda_r \end{bmatrix}. \tag{52}$$

The matrix differential operators Ξ and Ψ are defined as

$$\Xi^T = \begin{bmatrix} \dfrac{\partial}{\partial S}\mathbf{1} & \left(\dfrac{\partial r}{\partial S}\right)^\wedge \\ 0 & \dfrac{\partial}{\partial S}\mathbf{1} \end{bmatrix}, \quad \Psi = \begin{bmatrix} \dfrac{\partial}{\partial S}\mathbf{1} & 0 & 0 \\ 0 & \dfrac{\partial}{\partial S}\mathbf{1} & \mathbf{1} \end{bmatrix}, \tag{53}$$

and the geometric stiffness matrix Y has the form as

$$Y = \begin{bmatrix} 0 & 0 & -n^\wedge \\ 0 & 0 & -m^\wedge \\ n^\wedge & 0 & nr'^T - (n^Tr')\mathbf{1} \end{bmatrix}, \tag{54}$$

where $r' = \frac{\partial r}{\partial S}$. The detailed derivation can be found in Simo and Vu-Quoc [48] or our previous works [30,53].

The linear part caused by the applied distributed load δG_a in Eq. (49) can be given by

$$\delta G_a\left[\Phi^{(i)}_{n+1}, \delta\Phi\right] = -\int_0^L \delta\Phi^T\left(\widetilde{q}_g + \widetilde{q}_m\right)\Delta\Phi^{(i)}_{n+1}dS, \tag{55}$$

where q_g and q_m are the tangent load stiffness matrix corresponding to the gravity loads and magnetic driving forces and have the expressions as

$$q_g = \rho A_s\begin{bmatrix} 0 & 0 \\ 0 & g^\wedge\xi^{c\wedge} \end{bmatrix}, \quad q_m = \frac{A_s}{\mu_m}\begin{bmatrix} 0 & -(\nabla B_0)^T(\Lambda_rB_r)^\wedge \\ (\Lambda_rB_r)^\wedge\nabla B_0 & B_0^\wedge(\Lambda_rB_r)^\wedge \end{bmatrix}. \tag{56}$$

The linear part caused by the dynamical part δG_a in Eq. (49) can be given by

$$\delta G_d = \int_0^L \delta\Phi^T(\widetilde{H}_1 + \widetilde{H}_2)\Delta\Phi^{(i)}_{n+1}dS, \tag{57}$$

where H_1 and H_2 are the tangent dynamic stiffness matrices, and adopts the form

$$H_1 = \left\{\begin{array}{cc} \dfrac{\rho A_s}{\beta h^2}\mathbf{1} & 0 \\ 0 & \Lambda_r\left[\dfrac{J_\rho}{\beta h^2} - \dfrac{\gamma}{\beta h}(J_\rho W)^\wedge + \dfrac{\gamma}{\beta h}W^\wedge J_\rho\right]\Lambda^T_{r(n)}Z(\theta) - [\Lambda_r(J_\rho\dot{W} + W^\wedge J_\rho W)]^\wedge \end{array}\right\}, \tag{58}$$

$$H_2 = \rho A_s\left\{\begin{array}{cc} 0 & -\Lambda_r\left[\dfrac{\xi_0^{c\wedge}}{\beta h^2} + \dfrac{\gamma}{\beta h}(W^\wedge\xi_0^c)^\wedge + \dfrac{\gamma}{\beta h}W^\wedge\xi_0^c\right]\Lambda^T_{r(n)}Z(\theta) - [\Lambda_r(\dot{W}^\wedge\xi_0^c + W^\wedge W^\wedge\xi_0^c)]^\wedge \\ \dfrac{\xi^{c\wedge}}{\beta h^2} & \ddot{r}^\wedge\xi^{c\wedge} \end{array}\right\}.$$

The matrix H_1 is referred to as the classical tangent dynamic stiffness matrix [63] and is caused by the linear and angular momentum relative to the centroids. The non-conventional tangent dynamic stiffness matrix H_2 represents the effect of the deviation of the center of mass from the geometric centroid on the dynamic.

3.4. Spatial discretization

Considering a classical spatial discretization, the approximations of the displacement increment field can be given by

$$\Delta \boldsymbol{r}_{n+1}^{(i),h} \simeq \sum_{I=1}^{n_n} N_I \Delta \boldsymbol{r}_{n+1,I}^{(i),h}, \quad \Delta \boldsymbol{\vartheta}_{n+1}^{(i),h} \simeq \sum_{I=1}^{N_n} N_I \Delta \boldsymbol{\vartheta}_{n+1,I}^{(i),h}, \tag{59}$$

where n_n is the total number of the nodes; N_I is the shape functions associating with the node I; $\Delta \boldsymbol{r}_{n+1,I}^{(i),h}$ and $\Delta \boldsymbol{\vartheta}_{n+1,I}^{(i),h}$ are the approximations of the displacement increment field at the node I. In this work, the variable superscript h represents the spatial discrete approximation of the variable. Following the Galerkin finite element method, the test functions $\delta \boldsymbol{\Phi}$ are approximated by the same manner as Eq. (59), and the spatially discrete version of the linearization of weak form can be given by

$$L(G^h) = \sum_{I=1}^{n_n} \sum_{J=1}^{n_n} \delta \boldsymbol{\Phi}_I^{hT} \left(\boldsymbol{P}_I + \boldsymbol{K}_{IJ} \Delta \boldsymbol{\Phi}_{n+1,J}^{(i),h} \right) = 0, \tag{60}$$

where $\boldsymbol{K}_{IJ}$ are the stiffness submatrices coupling node I and J, and are represented as

$$\boldsymbol{K}_{IJ} = \boldsymbol{R}_{IJ} + \boldsymbol{q}_{IJ} + \boldsymbol{H}_{IJ}. \tag{61}$$

The stiffness submatrices caused by the resultant force and moment $\boldsymbol{R}_{IJ}$ can be given by

$$\boldsymbol{R}_{IJ} = \int_0^L \left(\widetilde{\boldsymbol{\Xi}}_I^h \widetilde{\boldsymbol{d}}^h \widetilde{\boldsymbol{\Xi}}_J^{hT} + \widetilde{\boldsymbol{\Psi}}_I^h \widetilde{\boldsymbol{Y}}^h \widetilde{\boldsymbol{\Psi}}_J^{hT} \right) dS, \tag{62}$$

where the operators $\widetilde{\boldsymbol{\Xi}}_I^h$ and $\widetilde{\boldsymbol{\Psi}}_I^h$ are

$$\widetilde{\boldsymbol{\Xi}}_I^h = \begin{bmatrix} N_I' \mathbf{1} & \mathbf{0} \\ -N_I \left(\dfrac{\partial \boldsymbol{r}^h}{\partial S} \right)^{\wedge} & N_I' \mathbf{1} \end{bmatrix}, \quad \widetilde{\boldsymbol{\Psi}}_I^h = \begin{bmatrix} N_I' \mathbf{1} & \mathbf{0} & \mathbf{0} \\ \mathbf{0} & N_I' \mathbf{1} & N_I \mathbf{1} \end{bmatrix}. \tag{63}$$

The $\widetilde{\boldsymbol{d}}^h$ and $\widetilde{\boldsymbol{Y}}^h$ are the spatial discrete approximation of $\widetilde{\boldsymbol{d}}$ and $\widetilde{\boldsymbol{Y}}$. The stiffness submatrices caused by the applied distributed load $\boldsymbol{q}_{IJ}$ have the form as

$$\boldsymbol{q}_{IJ} = -\int_0^L \left(\widetilde{\boldsymbol{q}}_g^h + \widetilde{\boldsymbol{q}}_m^h \right) N_I N_J dS. \tag{64}$$

And the stiffness submatrices caused by the dynamical part $\boldsymbol{H}_{IJ}$ can be given by

$$\boldsymbol{H}_{IJ} = \int_0^L \left(\widetilde{\boldsymbol{H}}_1^h + \widetilde{\boldsymbol{H}}_2^h \right) N_I N_J dS. \tag{65}$$
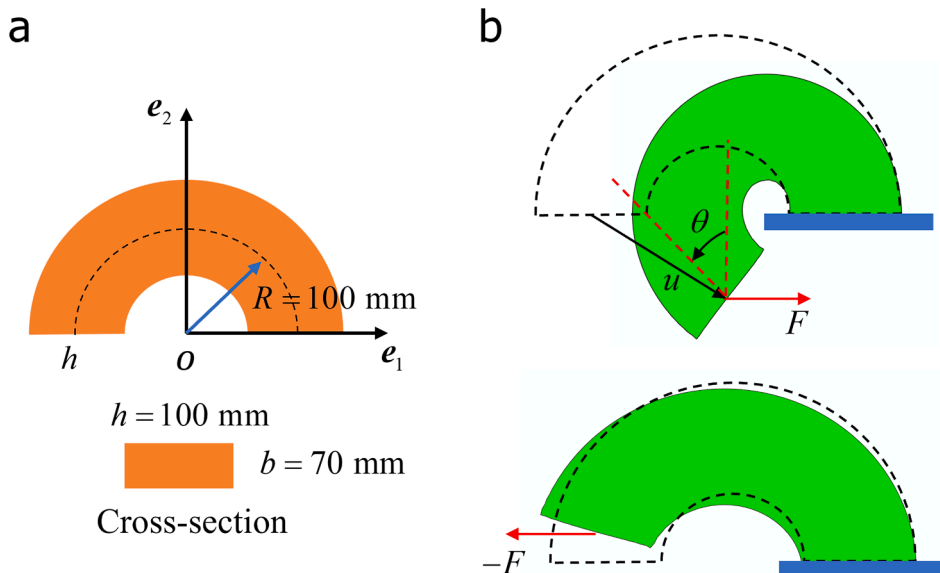

Fig. 2. Schematic of the semicircular cantilever subjected to end load: (a) undeformed shape of the semicircular cantilever. The radius of the semicircular cantilever is 100 mm, and the cross-section of the semicircular cantilever is a rectangle with a height of 100 mm and thickness of 70 mm; (b) deformed shapes under end loads in different directions.

Finally, the out-of-balance force coupling node I, $\boldsymbol{P}_I$ is

$$
\boldsymbol{P}_I = \int_0^L \left\{ \widetilde{\boldsymbol{\Xi}}_I^h \begin{bmatrix} \boldsymbol{n}^h \\ \boldsymbol{m}^h \end{bmatrix} - N_I \begin{bmatrix} \overline{\boldsymbol{n}}_g^h + \overline{\boldsymbol{n}}_m^h + \overline{\boldsymbol{n}}_o^h \\ \overline{\boldsymbol{m}}_g^h + \overline{\boldsymbol{m}}_m^h + \overline{\boldsymbol{m}}_o^h \end{bmatrix} \right\} dS
$$
$$
+ \int_0^L N_I \begin{bmatrix} \rho A_s \ddot{\boldsymbol{r}}^h + \rho A_s \dot{\boldsymbol{w}}^h \times \boldsymbol{\xi}^{ch} + \rho A_s \boldsymbol{w}^h \times \left(\boldsymbol{w}^h \times \boldsymbol{\xi}^{ch} \right) \\ \boldsymbol{I}_\rho^h \dot{\boldsymbol{w}}^h + \boldsymbol{w}^h \times \boldsymbol{I}_\rho^h \boldsymbol{w}^h + \rho A_s \boldsymbol{\xi}^{ch} \times \ddot{\boldsymbol{r}}^h \end{bmatrix} dS. \tag{66}
$$

4. Model validation

Three numerical examples are presented in this section and are compared with the 2D solid finite element simulation results and the results presented in the literature to further assess our model. The reduced integration is utilized to avoid the shear locking of the geometrically exact rod element [48], and the convergence criteria follow our previous work [53].

4.1. Example 1: semicircular cantilever subject to end load

We start with a semicircular cantilever of radius $R = 100$mm with the rectangle cross-section of height $h = 100$mm and thickness $b = 70$mm, as shown in Fig. 2(a). A concentrated force in the e_1-direction F is applied to the end of the cantilever, and the deformed
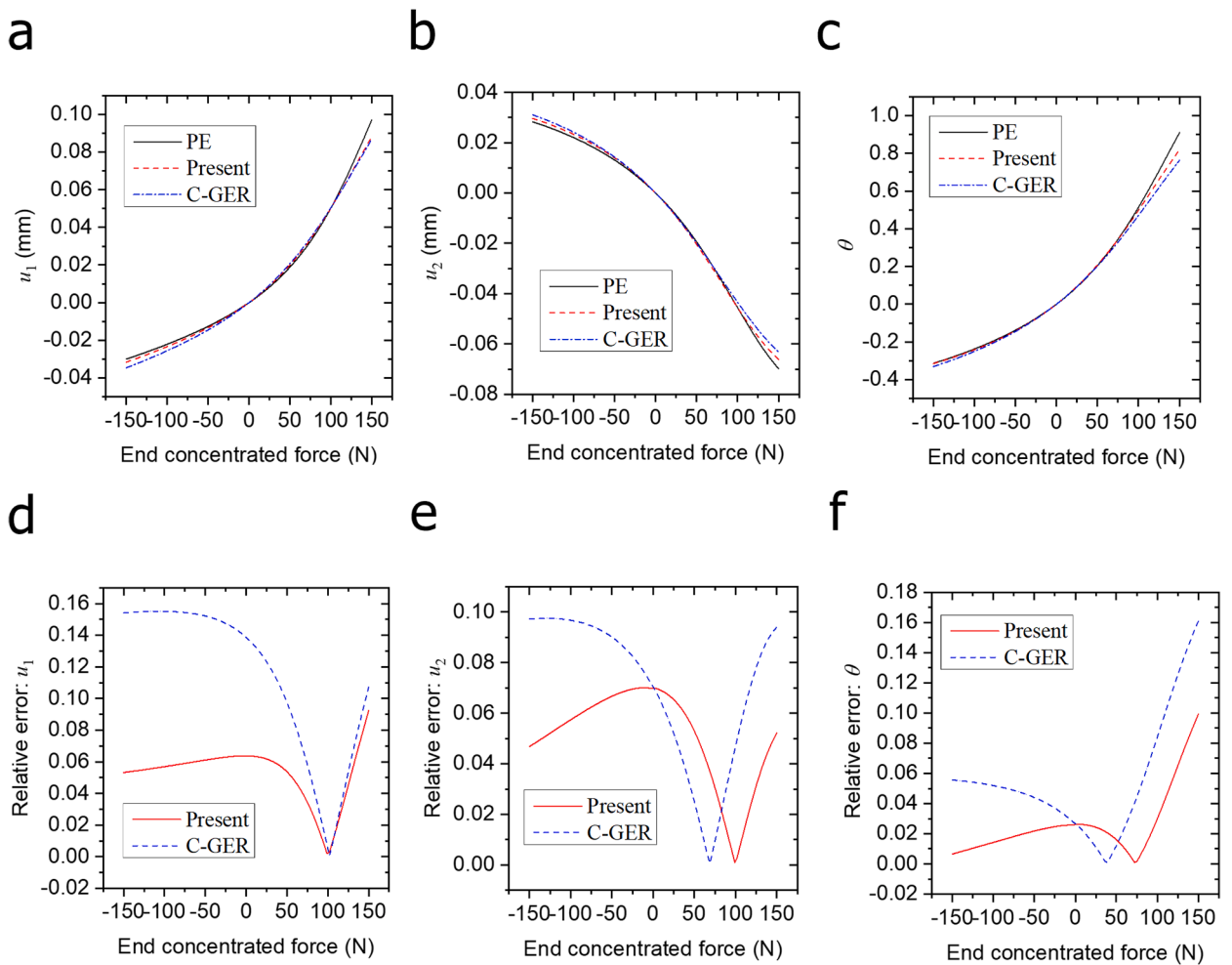
Fig. 3. Components of the displacement, rotation angle, and their relative error of the semicircular cantilever subjected to end load versus applied load. The black lines denote the results obtained by plane strain (PE) element formulation, red lines denote the results obtained by present element formulation, and blue lines denote the results obtained by classical geometrically exact rod (C-GEB) element formulation: (a) horizontal displacement; (b) vertical displacement; (c) rotation angle; (d) relative error of horizontal displacement; (e) relative error of vertical displacement; (f) relative error of rotation angle.

shapes of the cantilever are depicted in Fig. 2(b). We denote the displacement of the end by *u* and the rotation angle of the end by θ. Young's modulus of the rod is 1 MPa, and Poisson's ratio is 0. The end concentrated force slowly varies from −150 N to 150 N, which can be regarded as quasi-static. Furthermore, three element formulations are considered: the present rod element, the classical geometrically exact rod (C-GER) element, and the plane strain (PE) element. In finite element analysis, 12 two-node linear rod elements or 1521 four-node quadrilateral and 35 three-node tetrahedral PE elements are utilized to solve this problem. The components of the displacement of the end u_1 and u_2 obtained by the three methods can be found in Fig. 3(a) and (b), and the rotation angle θ can be found in the Fig. 3(c). We calculate the relative error of the displacement components and the rotation angle relative to the results obtained by PE finite element analysis, which is shown in Fig. 3(d–f).

As shown in Fig. 3, the results obtained by the present rod model agree well with the results obtained by the PE finite element analysis, the relative error is within 10 %. However, there is a deviation between the results obtained by our model and the results obtained by PE finite element analysis, and it increase with the load. One possible explanation for the deviation could be the failure of the rigid cross-section assumption when subjected to significant loads. Compared to the C-GER model, the relative errors of the results obtained by our model are generally smaller, which means our model is more accurate in predicting the deformation of the curved rod. Considering that less elements are used in our formulation, we may conclude our model is efficient and accurate for predicting the deformation of curved rods. However, it must be mentioned that the differences between the results obtained from the present model and C-GER model are small even for such a large-curvature rod. This means that the influence of the tension-bending and shear-torsion coupling effects is negligible, especially for small- or medium-curvature rods.

4.2. Example 2: large displacement vibration of the elbow cantilever

In this numerical example, we consider an elbow cantilever with two legs, each of which has the length $L = 10\text{m}$, as shown in Fig. 4. The elbow cantilever is subjected to an out-of-plane force load $\boldsymbol{F} = F\boldsymbol{e}_2$ at its elbow, and the magnitude of the out-of-plane load F follows the pattern of a hat function, as shown in Fig. 4. The stiffness properties of the rod are $EA = \mu A_1 = \mu A_2 = 10^6\text{N}$ and $EI_1 = EI_2 = \mu J = 10^3\text{N} \cdot \text{m}^2$. In order to emphasize the influence of the rotational motion, the inertia constants of the rod are artificially chosen to be $\rho A = 1\text{kg} \cdot \text{m}^{-1}$ and $\rho I_1 = \rho I_2 = 10\text{kg} \cdot \text{m}$.

This example has been investigated by a series of studies [49,63] using the C-GER model. The cantilever undergoes a large displacement vibration of the same order as the length of the cantilever. We utilize our formulation to simulate the vibration process with two meshes: (1) two quadratic elements (2) and ten quadratic elements. In the calculation, we adopt the time step size as $h = 0.25\text{s}$ and the trapezoidal rule (β = 0.25and γ = 0.5) to analyze the motion of the cantilever from τ = 0s to τ = 30s. The e_2-direction displacement component u_2 at the elbow and the end are shown in Fig. 5(a), and the deformed shapes of the cantilever are shown in Fig. 5(b). Our results show great agreement with the results reported in the literature [49,63], which proves the ability of our implementation to predict the dynamic response of the rod. It should be noted that the legs of the elbow cantilever are straight rods whose initial curvature is zero. Therefore, the present model and the C-GER model are identical in this case.

4.3. Example 3: the dynamic snap-through behavior of a bistable arch

This example was first analytically and experimentally investigated by Tan et al. [61], afterwards Stewart et al. [21] utilized a magneto-viscoelastic model to simulate it. The bistable arch is a straight rod of length $L_0 \approx 120.5\text{mm}$ at the initial configuration, and it is compressed on both ends to form an arch with span $L = 120\text{mm}$ and rise $a \approx 4\text{mm}$, as shown in Fig. 6(a). The cross-sections of the arch are rectangles of width $W = 20\text{mm}$ and thickness $H = 2.5\text{mm}$. The arch is made from a mixture of the polydimethylsiloxane
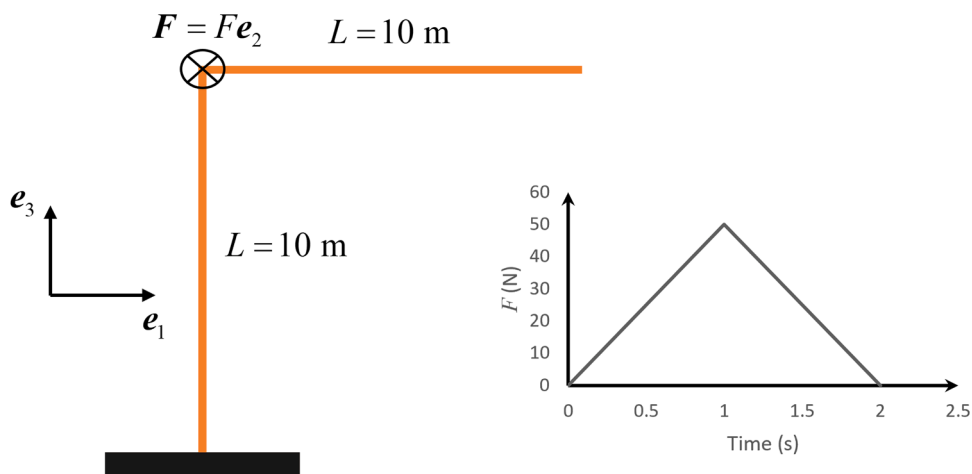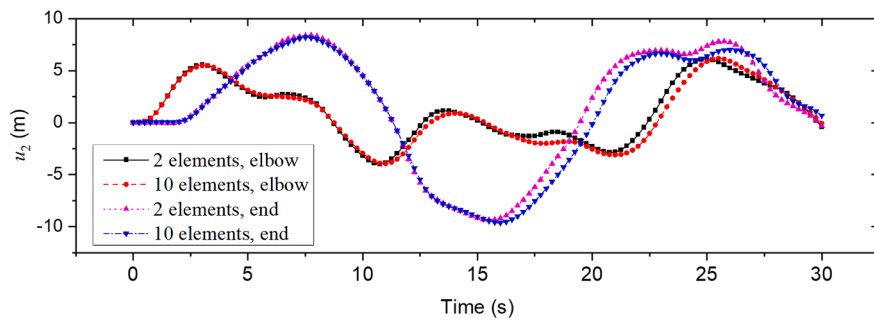

Fig. 4. Schematic of the elbow cantilever subjected to out-of-plane force load and the time signal of the force load. The length of each leg of the elbow cantilever is 10 m, and the elbow cantilever is subjected to an e_2-direction concentration force.
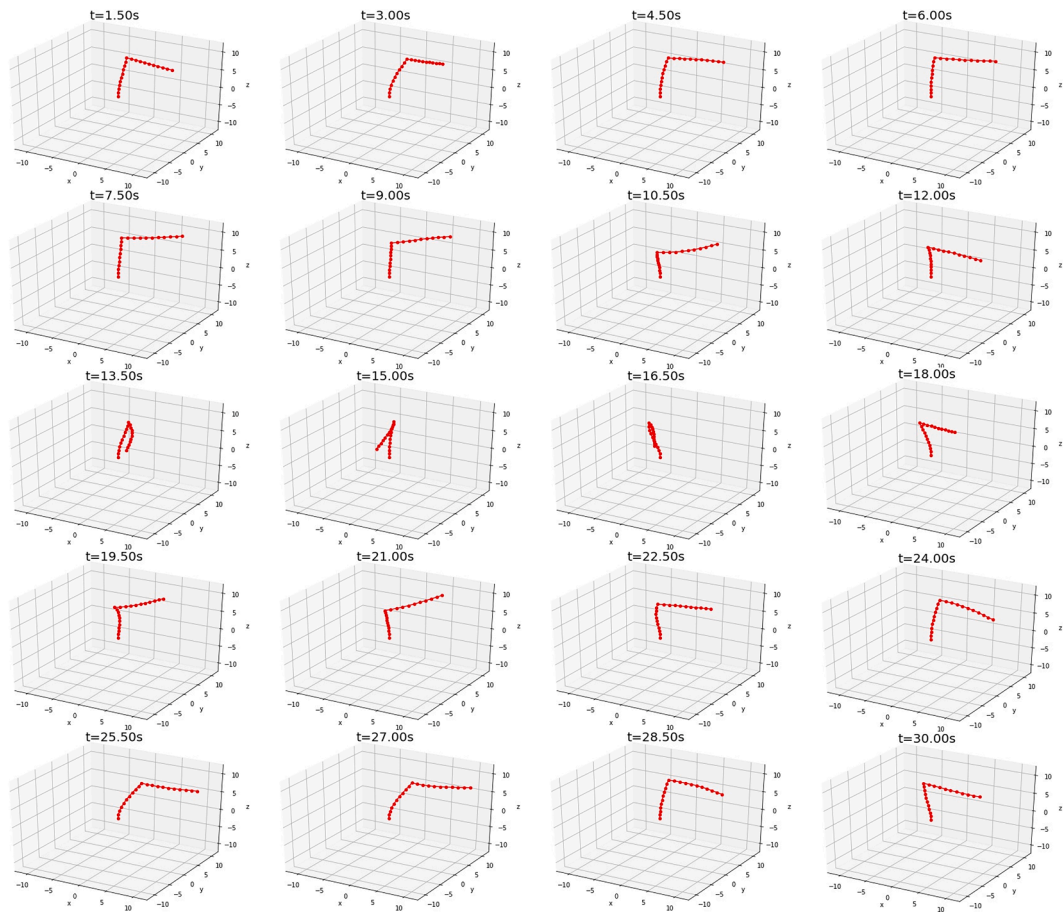
a

b

Fig. 5. Large displacement vibration of the elbow cantilever subjected to out-of-plane force load: (a) the out-of-plane displacement at the elbow and the end versus time with two meshes. (b) deformed shapes.

(PDMS) matrix and NdFeB particles with an equal mass fraction, with the residual magnetic flux density $\boldsymbol{B}_r = B_r\boldsymbol{e}_3$ parallel to the axial direction as shown in Fig. 6(a). It should be noted that the residual magnetic flux density is discontinuous at the midpoint. When the arch is subjected to a large enough applied magnetic flux density $\boldsymbol{B}_a = B_a\boldsymbol{e}_1$ in the $\boldsymbol{e}_1$-direction, a rapid dynamic transition or "snap-through" between two buckled configurations will be triggered, as shown in Fig. 6(a), and the minimum applied magnetic flux density which can trigger the snap-through is called as the "critical applied magnetic flux density" $\boldsymbol{B}_a^{cr} = B_a^{cr}\boldsymbol{e}_1$.

Tan et al. [61] adopted the applied magnetic flux density on the arch by three different loading modes: (1) DC pulse magnetic field, (2) constant magnetic field, and (3) triangle magnetic field, and they reported the displacement data of the midpoint of the arch. In this subsection, our model is used to simulate the dynamic response of the arch to the three kinds of loads, and the results obtained by our model are compared with the experiment data reported by Tan et al. [61] to assess our model. The experiment data can be found in the
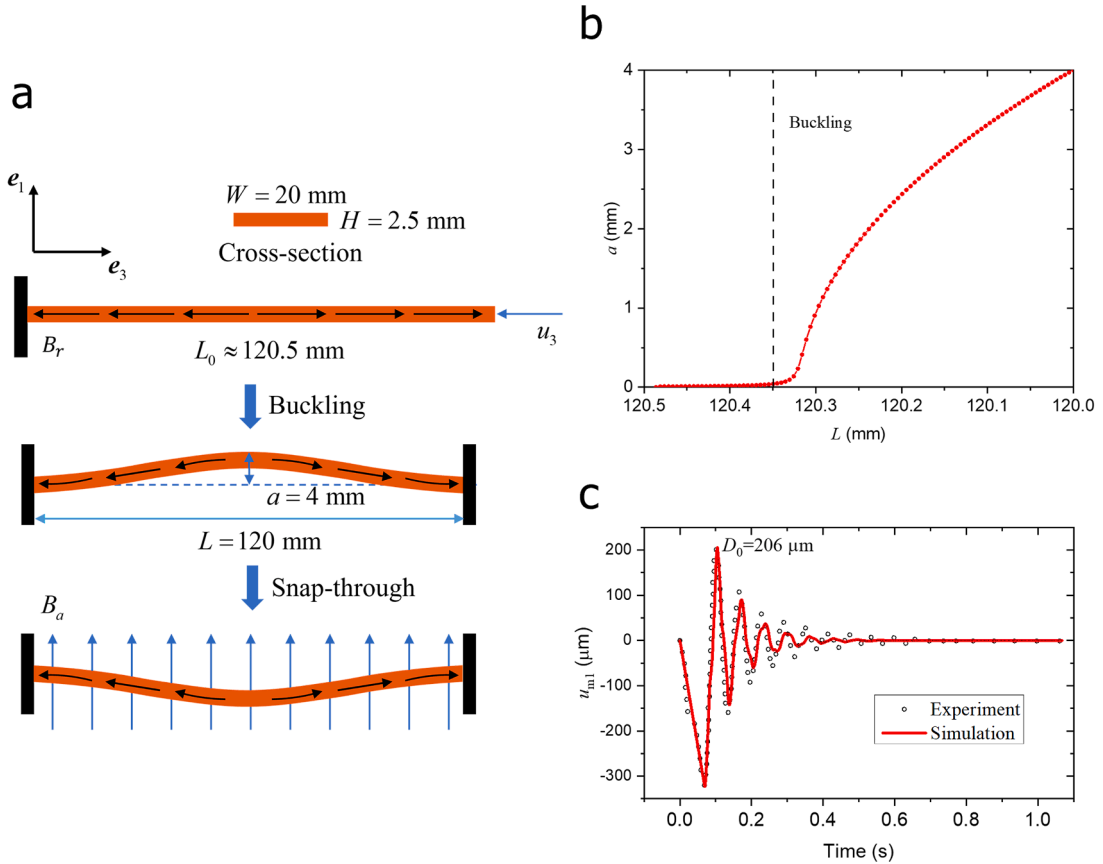
Fig. 6. The bistable hard-magnetic soft arch: (a) the snap-through behavior of the bistable arch. The arch is a straight rod with an initial length of about 120.5 mm in the initial configuration, and the cross-sections of the arch are rectangles of width 20 mm and thickness 2.5 mm. The residual magnetic flux density of the arch is parallel to the e_3-direction is shown. The straight rod is compressed on both ends to form an arch with a rise of about 4 mm and a span of 120 mm. When a large enough applied magnetic flux density in e_1-direction is applied on the arch, the arch will rapidly transit into another buckled configuration, called as "snap-through"; (b) the rise of the arch versus the span of the arch; (c) the time signal of the displacement of the midpoint of the arch in the e_1-direction obtained by Tan et al. [61] and simulation. The first peak of the time signal obtained by simulation D_0 is 206 μm.

Data Availability section in [21].

Young's modulus of the arch is 4.2 MPa, Poisson's ratio is 0.3, and the magnitude of the residual magnetic flux density $B_r = 72.3$mT, which are obtained from [61]. It should be noted that the residual magnetic flux density is not given directly in [61], and can be calculated by Eq. (24) of [61]. The density of the arch is estimated as 1733.5 Kg/m³ according to the components of the material. The aforementioned material parameters obtained by test experiments are referred to as "initial parameters". To achieve the accurate prediction of the dynamic snap-through behavior, we slightly adjust the initial parameters to fit the experimental data of the arch under the DC pulse magnetic field, and the new group of material parameters are referred to as "modified parameters" (detailed description is in Section 4.3.1). To demonstrate the ability of our model to predict the dynamic snap-through behaviors, we use the two groups of material parameters to simulate the dynamic snap-through behaviors of a bistable arch under two other kinds of magnetic fields (constant and triangle magnetic field), and the simulation results are compared with the experiment results.

In the beginning, we simulate the compression process of the straight rod of the initial length $L_0 = 120.486$mm to obtain the buckled configuration depicted in Fig. 6(a). In the simulation process, we choose to with the time step size of 100000s so that the inertial effect is negligible, and the process can be regarded as quasi-static. We integrated the problem with 100 time steps. Eleven quadratic elements are used in this example. To make sure we obtain the desired buckled configuration, a very small force of 0.0001 N in e_1-direction is applied at the midpoint of the arch in the first 90 steps. The relation between the rise a and the span L of the arch can be found in Fig. 6(b). The buckling occurs after $L = 120.35$mm.

For dynamic analysis of the arch, the environmental damping and viscoelasticity play a role. We apply a linear translational damping constraint with the same linear coefficient C_{damp} at every node to capture the effects, and the load f_{damp} and additional stiffness K_{damp} resulted from the damping constraint can be given by

$$\boldsymbol{f}_{\text{damp}} = C_{\text{damp}}\dot{\boldsymbol{r}}_{\text{damp}},$$

$$\boldsymbol{K}_{\text{damp}} = \frac{\gamma C_{\text{damp}}}{\beta h}\boldsymbol{I}, \tag{67}$$

where $\dot{\boldsymbol{r}}_{\text{damp}}$ is the velocity of the point at which the damping constraint is applied. It should be noted that the method to capture the viscous effect is an engineering simplification.

Tan et al. [61] gave the time signal of the displacement of the midpoint of the arch in the e_1-direction u_{m1} after a small perturbation, given in Fig. 6(c). We use the first peak of the time signal $D_0 = 201\mu m$ to calibrate the linear coefficient. We apply a displacement of 0.032 mm at the midpoint of the arch at a time step of 0.069 s as a perturbation and adjust the linear coefficient of the damping constrain to make the time signal of u_{m1} obtained by simulation have the close first peak D_0 as it given by Tan et al. [61]. We find the first peak $D_0 = 206\mu m$ obtained by simulation with $C_{\text{damp}} = 0.011\text{kg}/\text{s}$ matches well with the experimental results, and the simulation results are given in Fig. 6(c). It can be obviously found in Fig. 6(c) that the attenuation ratio decreases as the displacements decreases which should be constant for linear damping constraint. It means that the linear translational damping constraint can not completely
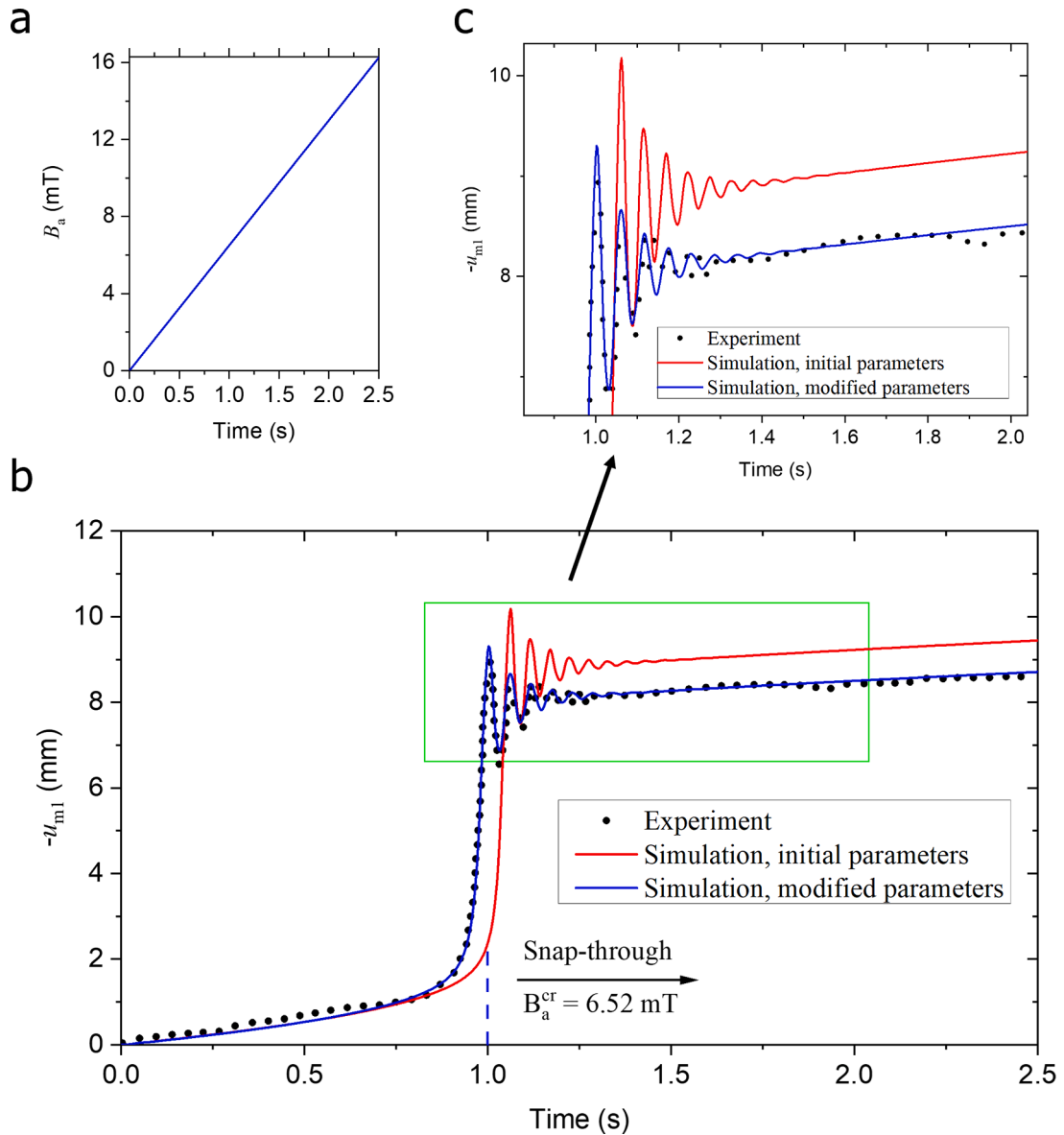

Fig. 7. The bistable arch subjected to a DC pulse magnetic field: (a) Time signal of the DC pulse magnetic field; (b) the negative value of the displacement of the midpoint of the arch in the e_1-direction obtained by the experiment [61] and the simulations with initial or modified parameters; (c) Partial enlarged view of (b).

depict the viscous effect, especially for very small displacements. However, the scale of the displacements in the snap-through behaviors is far larger than it in the damped oscillation of the arch. The simplification of the viscous effects may be appropriate for the snap-through behaviors of the arch, and comparison between subsequent experiment and simulation results also indicates this.

4.3.1. DC pulse magnetic field

As shown in Fig. 7(a), a DC pulse magnetic field B_a in the e_1-direction was increased from 0 mT to 16.3 mT with a speed of 6.5 mT/s, and it is applied to the arch. Fig. 7(b) and (c) record the negative values of the displacement of the midpoint of the arch in the e_1-direction, denoted by $-u_{m1}$ in response to such a magnetic field obtained by experiment [61] and simulation. The critical applied magnetic flux density obtained by simulation$B_a^{cr} = 6.52$mT is very close to the one obtained from the experiment, i.e., 6.3 mT. For dynamic analysis, our model captures the oscillation phenomenon, and we consider the first and second peaks in the oscillation process. The period and the ratio of the amplitude attenuation predicted by simulation are 0.055 s and 1.08, respectively. The corresponding values are 0.06 s and 1.07 reported by Tan et al. [61]. Our model gives a good prediction of the period and the ratio of amplitude attenuation. During the stage (i.e., 1.5 s – 2.5 s), the displacements obtained by the simulation are about 10 % larger than the experimental data, and this mismatch also occurred in the results obtained by the theoretical model of Tan et al. [61]. We think this deviation may be caused by the experimental error, such as the measurement accuracy of the initial rise a. As will be shown, the deviation of the initial rise $a$from the reported data, that is 4 mm, will affect the stiffness of the arch.

Stewart et al. [21] applied a magneto-viscoelastic model to simulate this example with the modified initial rise $a^* = 3.72$ and the modified residual magnetic flux density $B_r^* = 67.5$mT, and their simulation results showed a good agreement with the experimental data. Inspired by this, we calibrate the material parameters, including the initial rise and the residual magnetic flux density, to match the experimental data of the dynamic response of the arch to the DC pulse magnetic field. We find that using the modified initial rise $a^* = 3.66$mm and the modified residual magnetic flux density $B_r^* = 60$mT leads to an improved result in comparison with the experimental data. The simulation results with modified parameters are shown in Fig. 7(b) and (c). In the subsequent sections, we further investigate the motion of the arch with the other two loading modes using both the initial parameters and the modified parameters.

4.3.2. Constant magnetic field

In this case, a constant magnetic field in the e_1-direction of $B_a = 7$mT is applied to the arch, as is shown in Fig. 8(a). The applied magnetic field is slightly above the critical applied magnetic fields $B_a^{cr} = 6.52$mT and the snap-through occurs. The experimental data [61] and the simulation results with the initial or modified parameters of the negative value of the displacement of the arch in e_1-direction $-u_{m1}$ are presented in Fig. 8(b). The simulations with initial or modified parameters both give a satisfactory prediction of the period, amplitude, and the ratio of amplitude attenuation. The deviation of the balancing position between the experimental data and the simulation data with the initial parameters is about 9 %.

4.3.3. Triangle magnetic field

A triangle magnetic field, shown in Fig. 9(a), is applied to the arch. The amplitude and period of the magnetic field are 16.3 mT and 10 s, respectively. The experimental data [61] and the numerical prediction with the initial and modified parameters of $-u_{m1}$ can be
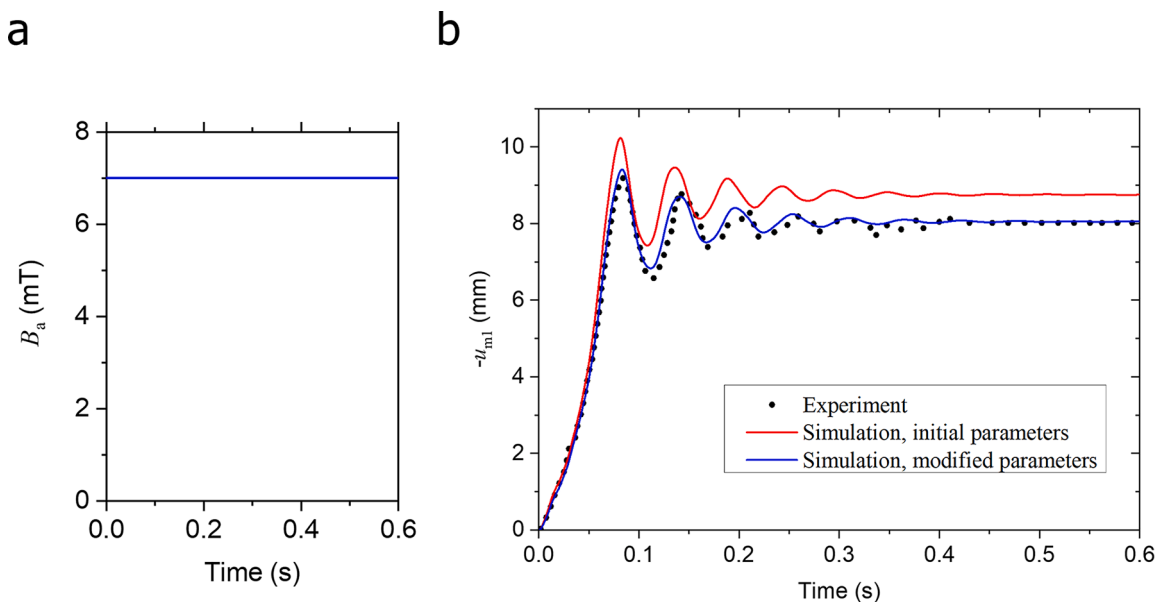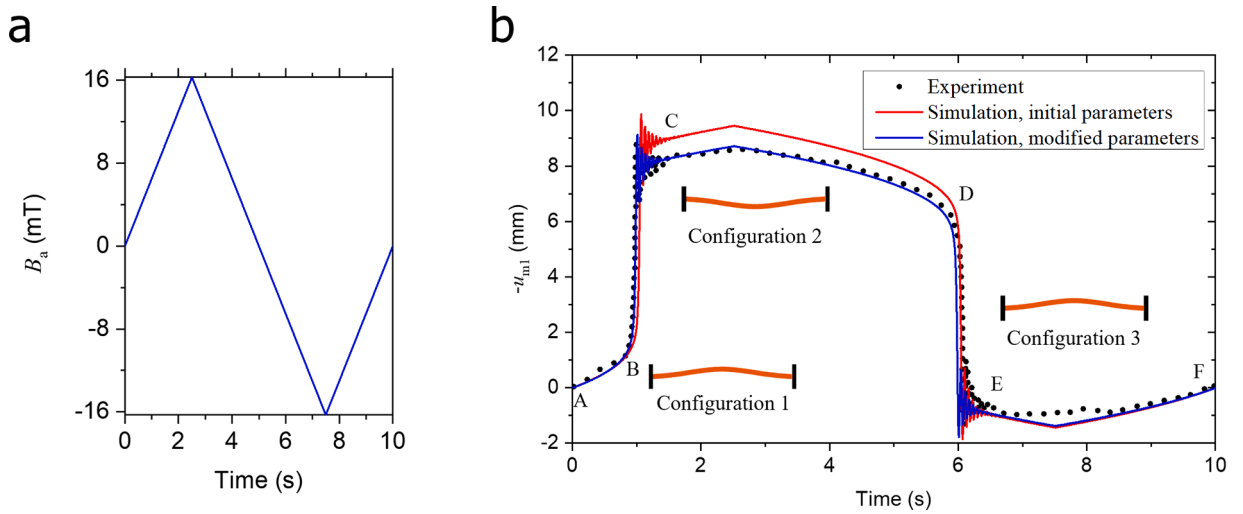

Fig. 8. The bistable arch subjected to a constant magnetic field of 7 mT: (a) Time signal of the constant magnetic field; (b) the negative value of the displacement of the midpoint of the arch in the e_1-direction obtained by experiment [61] and the simulations with initial or modified parameters.

Fig. 9. The bistable arch is subjected to a triangle magnetic field with an amplitude of 16.3 mT and a period of 10 s: (a) Time signal of the constant magnetic field; (b) the negative value of the displacement of the midpoint of the arch in the e_1-direction obtained by experiment [61] and the simulations with initial or modified parameters. The process can be divided into 2 snap-through stages (point B to C and point D to E) and 3 stable stages (point A to B with configuration 1, point C to D with configuration 2, and point E to F with configuration 3).

found in Fig. 9(b). As shown in Fig. 9(b), The process can be divided into 5 stages: (1) the configuration of the arch is configuration 1 during the period delimited by points A and B; (2) the arch rapidly snap from point B to C; (3) the configuration of the arch is configuration 2 during the period delimited by point C and D; (4) the arch rapidly snap from point D to E; (5) the configuration of the arch is configuration 3 during the period delimited by point E and F. The simulation with the initial or modified parameters both give a great prediction of the five stages.

In general, the simulation results of the arch applied with the three kinds of magnetic fields using the initial and modified parameters both agree with the experimental data well, especially before the occurrence of the snap-through. The snap-through behavior of the arch can be predicted well by our model.

5. The motions of hard-magnetic soft robotic arm

In this section, we prepare a curved hard-magnetic soft robotic arm and apply the magnetic field in two directions to the robotic arm, respectively. Our model is utilized to predict the motions of the HMS robotic arm, and the simulation results are compared with the experiment results.
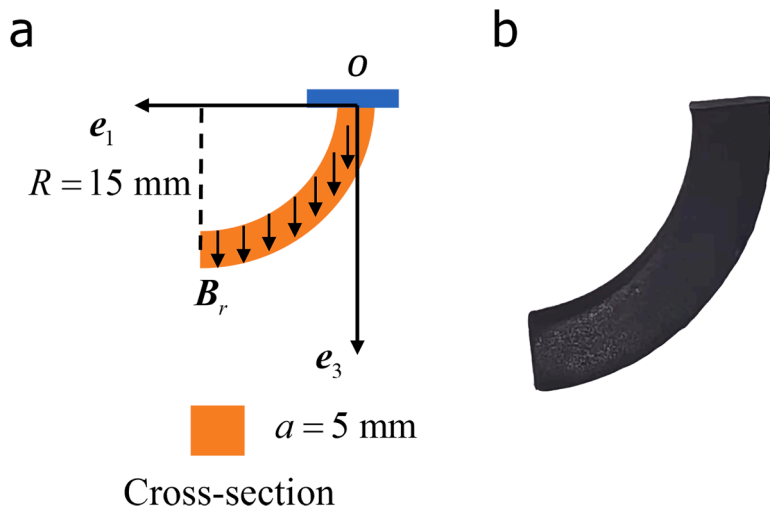
Fig. 10. Hard-magnetic soft robotic arm: (a) the schematic of the hard-magnetic soft robotic arm; (b) the physical image of the hard-magnetic soft robotic arm.

5.1. Material preparation and characterization

The hard-magnetic soft material of the robotic arm is prepared by mixing the NdFeB powder with an average diameter of 5 μm and the silicon rubber E600 (Hong Ye Silicone). The two fillers of the mixture have the same mass fraction of 50 %. The mixture is poured into the mold and then cured for 12 h at room temperature to fabricate the HMS robotic arm. The robotic arm is a quarter arc cantilever with the radius of $R \approx 15$mm, and the cross-section of the robotic arm is a square with the side length of $a \approx 5$mm, as shown in Fig. 10 (a) and (b). After demolding, the robotic arm is magnetized in e_3-direction by applying a strong magnetic field, and the strong magnetic field is generated by a high magnetic field generator (Shen Zhen He Sheng Hui Electronics Co. Ltd).

Young's modulus of the material is $E = 171.4$kPa, which is the slope of the stress–strain curve. The stress-strain curve of the material is obtained by the uniaxial tensile experiments which are conducted on ESM303 force test stands (Mark-10). The material is assumed as incompressible, meaning the Poisson's ratio of the material is chosen as 0.5. The density of the material is $\rho = 1741.23$kg/m^3. The residual magnetic flux density of the material is $B_r = 77.11$mT, and the residual magnetic flux density is measured by using the following procedure. An axially magnetized straight square rod with a length of $L = 70$mm and side length of $b = 7$mm is fabricated, whose material component is the same as the robotic arm. We measure the surface magnetic flux density $\boldsymbol{B}_{surface}$ at the distance of $d = 0.1$mm above the center of the top surface by TM5100 Gaussmeter (Tunkia Co., Ltd). The rod is assumed as the uniformly magnetized body, and the residual magnetic flux density of the material can be calculated by the volume integration as

$$B_r = \frac{\pi \left| \boldsymbol{B}_{surface} \right|}{\left[\arctan\left(\frac{b^2}{2d\sqrt{2b^2 + 4d^2}} \right) - \arctan\left(\frac{b^2}{2(d+L)\sqrt{2b^2 + 4(d+L)^2}} \right) \right]}. \tag{68}$$

5.2. Experimental protocol

During experiments, the robotic arm is placed in a Helmholtz coil, which can induce a steady uniform magnetic field, as shown in Fig. 11(a) and (b). The coil is powered by a DC power source, and the magnitude of the magnetic field is measured by the Gaussmeter.
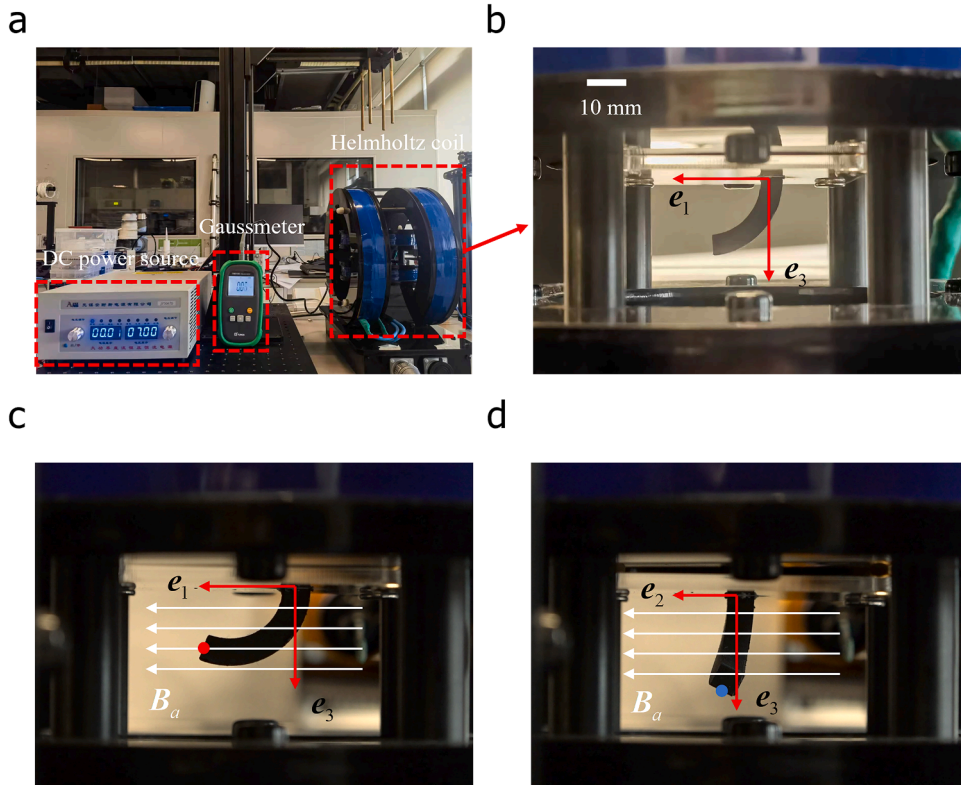

Fig. 11. The hard-magnetic soft robotic arm subject to the applied magnetic field: (a) the photograph of the full experimental apparatus; (b) the experimental setup for driving the robotic arm by applying the magnetic field; (c) the motion of the robotic arm subjected to an applied magnetic field in e_1-direction, and the displacements of the red point are measured; (d) the motion of the robotic arm subjected to an applied magnetic field in e_2-direction, and the displacements of the blue point are measured.

In our experiments, we apply the magnetic field in the e_1-direction and e_2-direction respectively to the robotic arm. When the magnetic field in the e_1-direction is applied to the robotic arm, the robotic arm will bend upwards in the e_1-e_2 plane, shown in Fig. 11(c), which are plane motions. Unlike this, the motions of the robotic arm under the applied magnetic field in e_2-direction are 3D motions, which include the bending and torsion, as shown in Fig. 11(d).

In our experiments, two kinds of loading processes are considered: (1) quasi-static loading, the applied magnetic flux density slowly increases from 0 mT to 10 mT (movie S1 and S2); (2) fast unloading, the applied magnetic flux density instantly decreases from 10 mT or 5 mT to 0 mT respectively (movie S3 - S6). The dynamic processes of the robotic arm are captured by a high-speed camera.

### 5.3. Simulation results vs experiment results

In this subsection, the predicted motion of the robotic arm by simulation is compared with the experiment results. When the applied magnetic field is in the e_1-direction, the displacements of the centroid of the end cross-section (red point in Fig. 11(c)) in the e_1-direction u_{c1} and the e_3-direction u_{c3} are measured. For the case of applying the magnetic field in the e_2-direction, the displacement of the midpoint of the lower edge of the end cross-section (green point in Fig. 11(c)) in the e_2-direction u_{m2} is measured. It should be noted the u_{m2} is not the same as u_{c2}, and they are related by

$$u_{m2} = u_{c2} + \frac{a}{2}(\Lambda_{\text{end}}\boldsymbol{e}_1)^T \boldsymbol{e}_2, \tag{69}$$

where Λ_{end} is the rotational matrix in the end cross-section. In the simulation process, ten quadratic elements are utilized, and gravity is considered. The experiment and simulation results of the quasi-static loading process are shown in Figs. 12(a) and (b). Our model accurately predicts the deformation of the HMS robotic arm without fitting any parameters from structural response.

To predict the dynamic motion of the HMS robotic arm, we capture the viscous effect by the linear damping constraint at every node, which is the same as the method in Section 4.3. We calibrate the coefficient of the linear damping constraint by the fast unloading process of the HMS robotic arm subjected to the applied magnetic flux density of 5 mT. We use the attenuation ratio between the first peaks D_0 and second peaks D_1 to calibrate the linear coefficient. It should be noted that the coefficients of the linear damping constraint are different in different directions, and the linear coefficient in e_i-direction is denoted by C_{damp}^i. We find that the attenuation ratio obtained by the simulation can match the experiment results with the linear coefficients $C_{\text{damp}}^1 = 0.0007 \text{kg}/\text{s}$, $C_{\text{damp}}^2 = 0.0010 \text{kg}/\text{s}$ and $C_{\text{damp}}^3 = 0.0007 \text{kg}/\text{s}$. The experiment results and simulation results are shown in Fig. 13.

In addition, we simulate the fast unloading process of the HMS robotic arm subjected to the applied magnetic flux density of 10 mT with the calibrated linear coefficients of the linear damping constraints. The simulation and experiment results are shown in Fig. 14. The period predicted by our model is 0.067 s and obtained by experiment is 0.053 s, which shows a good agreement. Due to the different periods, the phase difference between the experiment result and simulation result increases over time, resulting in an obvious deviation for a long duration. A possible reason causing errors in predicting period may be that the rigid cross-section assumption is made in our model. When the robotic arm undergoes high-speed motion, the inertial force will induce a severe distortion in cross-section, in which the rigid cross-section assumption maybe not hold. For the 2D dynamic motion, our model delivers a good prediction of the amplitude and the wave form, which means the linear damping constraints are appropriate for the 2D dynamical motion.
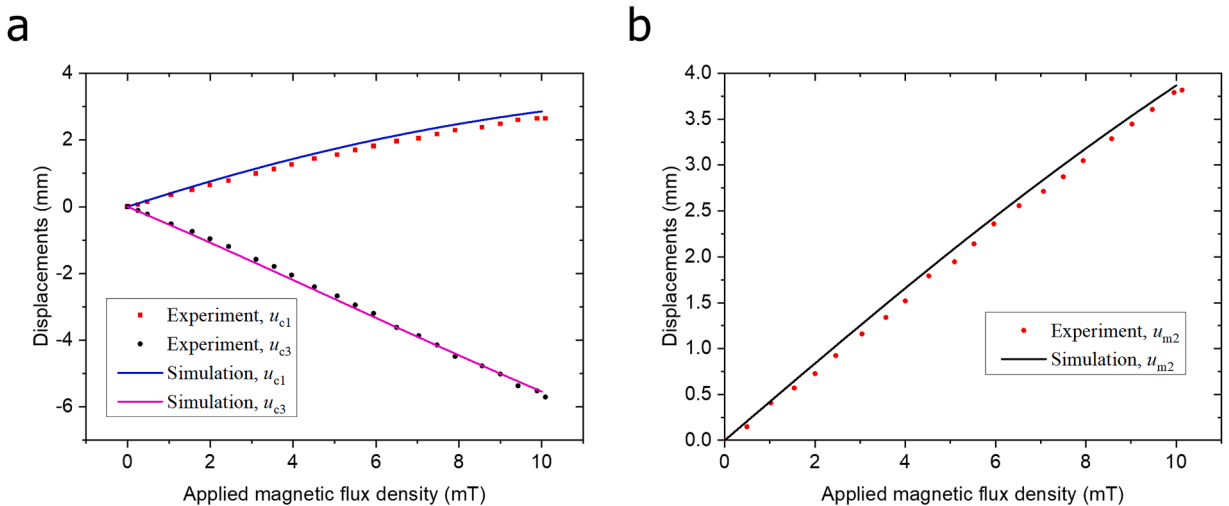
Fig. 12. The motion of the HMS robotic arm in the quasi-static loading process: (a) the displacements of end centroid of the HMS robotic subjected to an applied magnetic field in e_1-direction obtained by the experiment and simulation versus the applied magnetic flux density; (b) the displacements of midpoint of the lower edge of the HMS robotic subjected to an applied magnetic field in e_2-direction obtained by the experiment and simulation versus the applied magnetic flux density.
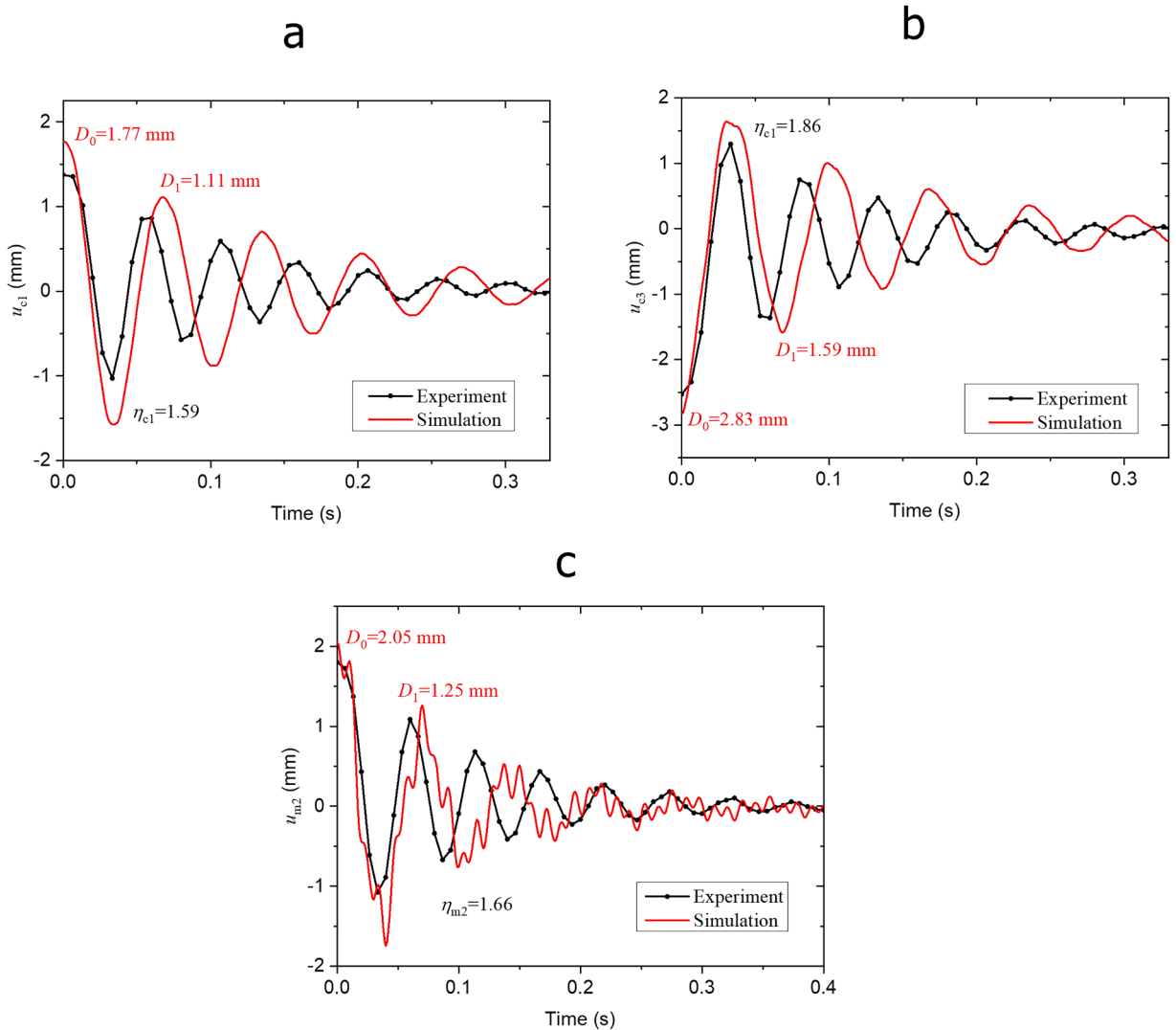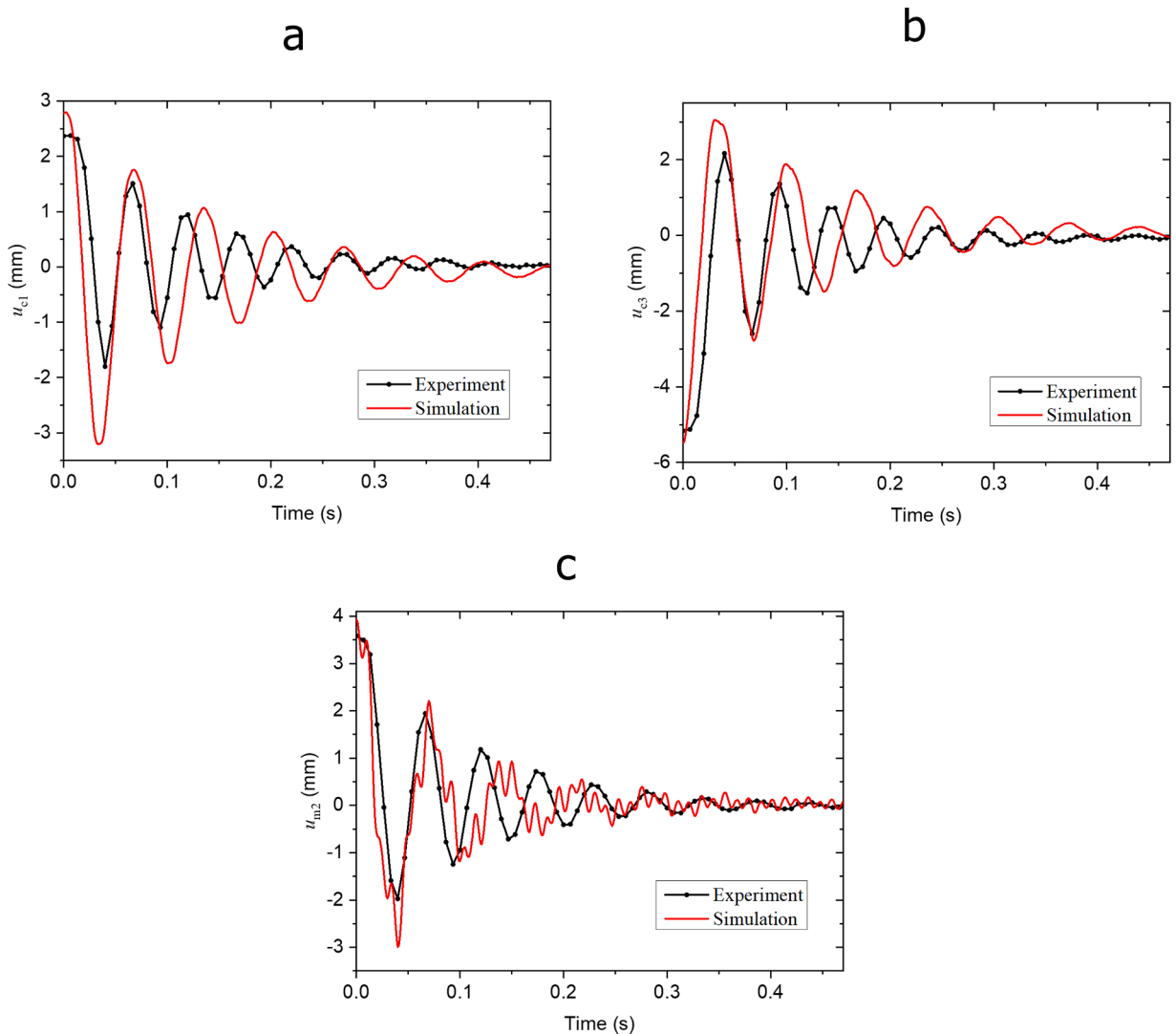
Fig. 13. The fast unloading process of the HMS robotic arm subjected to the applied magnetic flux density of 5 mT: (a) the displacements of the centroid of the end cross-section in the e_1-direction versus time. The first peak obtained by simulation is $D_0 = 1.77$ mm and the second peak obtained by simulation is $D_1 = 1.11$ mm. The attenuation ratio obtained by experiment is $\eta_{c1} = 1.59$; (b) the displacements of the centroid of the end cross-section in the e_3-direction versus time. The first peak obtained by simulation is $D_0 = 2.83$ mm and the second peak obtained by simulation is $D_1 = 1.59$ mm. The attenuation ratio obtained by experiment is $\eta_{c3} = 1.86$; (c) the displacements of midpoint of the lower edge of the end cross-section in the e_2-direction versus time. The first peak obtained by simulation is $D_0 = 2.05$ mm and the second peak obtained by simulation is $D_1 = 1.25$ mm. The attenuation ratio obtained by experiment is $\eta_{m2} = 1.66$.

However, the predicted wave form of 3D dynamical motion shows deviation from the measured wave form. The main reason is that using the linear translational damping constraint to capture the viscous effects is too simple for 3D-deformation. The linear translational damping constraint can't dissipate the energy of torsional motion, which plays an important role in the 3D-deformation. In addition, the self-inductance of the coils also affects the prediction of the motions of the HMS robotics arm. Due to the self-inductance of the coils, the magnetic flux density will not disappear instantly after closing the power supplement. In general, our model shows the ability to predict the motion of the HMS robotic arm.

6. Conclusion

In this work, we present a 3D curved rod model including the "tension-bending" and "shear-torsion" coupling effects to predict the dynamic motion of the hard-magnetic soft robotic arm. In our model, we define the effective deformation gradient of the deformed configuration relative to the undeformed curved configuration with the rigid cross-section assumption, as shown in Eq. (10). For isotropic linear elastic material, the constitutive equations of the rod (i.e., Eqs. (18) and (19)) are obtained by integrating the stress of the entire cross-section. With the initial curved configuration, two main load types of HMS robotic, i.e., gravity and magnetic loads, are

Fig. 14. The fast unloading process of the HMS robotic arm subjected to the applied magnetic flux density of 10 mT: (a) the displacements of the centroid of the end cross-section in the e_1-direction versus time; (b) the displacements of the centroid of the end cross-section in the e_3-direction versus time; (c) the displacements of midpoint of the lower edge of the end cross-section in the e_2-direction versus time.

formulated in our model, shown in Eqs. (29) and (34). To model the magnetic load, a rotation-based magnetic free energy density is applied to describe the material of the HMS robotic. It is worth mentioning that the gradient applied magnetic field is included in our model. In addition, the reduced balance equation is presented in Eq. (35). In Section 3, the finite element formulation and numerical implementation of the problem are presented. An implicit time stepping algorithm based on the classical Newmark algorithm is utilized to achieve the numerical time integration of the 3D finite rotations.

To validate our model, three simulation examples are presented in Section 4. The deformations of a semicircular cantilever subject to end load (Section 4.1), the large displacement vibration of the elbow cantilever (Section 4.2), and the dynamic snap-through behavior of a bistable arch (Section 4.3) are numerically studied by our model, and the simulation results are compared with the results reported in the literature, which show a satisfactory agreement. Furthermore, a series of experiments about the quarter arc HMS robotic arm are performed in Section 5. The robotic arm is subjected to applied magnetic field in two directions with two loading modes: (1) quasi-static loading; (2) fast unloading, and the simulation results and experiment results show great agreement.

Although our model performs reasonably well in predicting the motion of the HMS robotic arm, some limitations should be mentioned and further discussed: (1) The magnetic free energy density utilized in this work indicates the relation between the applied magnetic field and the magnetic flux density is linear, which means our model is not appropriate when the applied magnetic field is large. Besides, the dipole–dipole interactions are not included in our model. Although, our previous work [30] showed the impact of the effect on the motion of the HMS robotic is small, the effect cannot be ignored when the mass fraction of magnetic particles is very large. Therefore, developing the HMS rod model incorporating the nonlinear constitutive law and dipole–dipole interactions is worthy

of future investigation. (2) The distribution of applied magnetic field is known and unaltered in our model, which is a simplification. The deformation of the HMS robotics actually affects the distribution of the applied magnetic field. It is necessary to consider the electromagnetic field in the surrounding environment in our future work. (3) The method to capture the viscous effect in our work is an engineering simplification, which is inadequate for complex viscous effects, such as the significant viscoelasticity in certain HMS materials. Incorporating the viscoelasticity of HMS material and the nonlinear damping constraints into our model is a critical task. (4) The rigid cross-section assumption maybe inappropriate for soft rods undergoing high speed motion. Taking the deformable cross-section into account is also an attractive direction.

The model presented in this work can effectively and accurately predict the dynamic motion of the HMS robotic, which is valuable for the design and optimization of the HMS rod-like robotics.

CRediT authorship contribution statement

Xin Li: Conceptualization, Data curation, Formal analysis, Investigation, Methodology, Visualization, Writing – original draft. **Wenkai Yu:** Data curation, Investigation, Methodology, Visualization, Writing – review & editing. **Xiaoyan Zhu:** Data curation, Investigation, Visualization, Writing – review & editing. **Ju Liu:** Methodology, Writing – review & editing. **Hongyan Yuan:** Funding acquisition, Methodology, Project administration, Resources, Supervision, Writing – review & editing.

Declaration of competing interest

The authors declare that they have no known competing financial interests or personal relationships that could have appeared to influence the work reported in this paper.

Data availability

Data will be made available on request.

Acknowledgments

Supplementary materials

Supplementary material associated with this article can be found, in the online version, at doi:10.1016/j.apm.2024.05.044.

References

[1] H. Chung, A.M. Parsons, L. Zheng, Magnetically controlled soft robotics utilizing elastomers and gels in actuation: a review, Adv. Intell. Syst. 3 (2021) 2000186, https://doi.org/10.1002/aisy.202000186.
[2] M. Sitti, D.S. Wiersma, Pros and cons: magnetic versus optical microrobots, Adv. Mater. 32 (2020) 1906766, https://doi.org/10.1002/adma.201906766.
[3] Y. Kim, X. Zhao, Magnetic soft materials and robots, Chem. Rev. 122 (2022) 5317–5364, https://doi.org/10.1021/acs.chemrev.1c00481.
[4] W. Wang, Z. Yao, J.C. Chen, J. Fang, Composite elastic magnet films with hard magnetic feature, J. Micromech. Microeng. 14 (2004) 1321–1327, https://doi.org/10.1088/0960-1317/14/10/005.
[5] G.V. Stepanov, A.V. Chertovich, E.Yu. Kramarenko, Magnetorheological and deformation properties of magnetically controlled elastomers with hard magnetic filler, J. Magn. Magn. Mater. 324 (2012) 3448–3451, https://doi.org/10.1016/j.jmmm.2012.02.062.
[6] M. Furusawa, K. Maeda, S. Azukizawa, H. Shinoda, F. Tsumori, Bio-mimic motion of elastic material dispersed with hard-magnetic particles, J. Photopolym. Sci. Technol. 32 (2019) 309–313, https://doi.org/10.2494/photopolymer.32.309.
[7] P. Narayanan, R. Pramanik, A. Arockiarajan, Hard magnetics and soft materials—A synergy, Smart Mater. Struct. 33 (2024) 043001, https://doi.org/10.1088/1361-665X/ad2bd8.
[8] Z. Wang, D. Weng, Z. Li, L. Chen, Y. Ma, J. Wang, A magnetic-controlled flexible continuum robot with different deformation modes for vascular interventional navigation surgery, Actuators 12 (2023) 247, https://doi.org/10.3390/act12060247.
[9] E. Diller, J. Zhuang, G. Zhan Lum, M.R. Edwards, M. Sitti, Continuously distributed magnetization profile for millimeter-scale elastomeric undulatory swimming, Appl. Phys. Lett. 104 (2014) 174101, https://doi.org/10.1063/1.4874306.
[10] G.Z. Lum, Z. Ye, X. Dong, H. Marvi, O. Erin, W. Hu, M. Sitti, Shape-programmable magnetic soft matter, Proc. Natl. Acad. Sci. 113 (2016), https://doi.org/10.1073/pnas.1608193113.
[11] Y. Kim, G.A. Parada, S. Liu, X. Zhao, Ferromagnetic soft continuum robots, Sci. Robot. 4 (2019) eaax7329, https://doi.org/10.1126/scirobotics.aax7329.
[12] A. Alfadhel, J. Kosel, Magnetic nanocomposite cilia tactile sensor, Adv. Mater. 27 (2015) 7888–7892, https://doi.org/10.1002/adma.201504015.
[13] S. Padmanabhan, Z. Alam, A.K. Sharma, Tunable anti-plane wave bandgaps in 2D periodic hard-magnetic soft composites, Int. J. Mech. Sci. 261 (2024) 108686, https://doi.org/10.1016/j.ijmecsci.2023.108686.
[14] J. Sim, R.R. Zhao, Magneto-mechanical metamaterials: a perspective, J. Appl. Mech. 91 (2024) 031004, https://doi.org/10.1115/1.4063816.
[15] Z. Alam, S. Padmanabhan, A.K. Sharma, Magnetically tunable longitudinal wave band gaps in hard-magnetic soft laminates, Int. J. Mech. Sci. 249 (2023) 108262, https://doi.org/10.1016/j.ijmecsci.2023.108262.

[16] L. Descamps, D. Le Roy, C. Tomba, A. Deman, Magnetic polymers for magnetophoretic separation in microfluidic devices, Magnetochemistry 7 (2021) 100, https://doi.org/10.3390/magnetochemistry7070100.

[17] L. Lu, J. Sim, R.R. Zhao, Mechanics of hard-magnetic soft materials: a review, Mech. Mater. 189 (2024) 104874, https://doi.org/10.1016/j.mechmat.2023.104874.

[18] R. Zhao, Y. Kim, S.A. Chester, P. Sharma, X. Zhao, Mechanics of hard-magnetic soft materials, J. Mech. Phys. Solids 124 (2019) 244–263, https://doi.org/10.1016/j.jmps.2018.10.008.

[19] D. Garcia-Gonzalez, Magneto-visco-hyperelasticity for hard-magnetic soft materials: theory and numerical applications, Smart Mater. Struct. 28 (2019) 085020, https://doi.org/10.1088/1361-665X/ab2b05.

[20] S. Lucarini, M.A. Moreno-Mateos, K. Danas, D. Garcia-Gonzalez, Insights into the viscohyperelastic response of soft magnetorheological elastomers: competition of macroscopic versus microstructural players, Int. J. Solids Struct. 256 (2022) 111981, https://doi.org/10.1016/j.ijsolstr.2022.111981.

[21] E.M. Stewart, L. Anand, Magneto-viscoelasticity of hard-magnetic soft-elastomers: application to modeling the dynamic snap-through behavior of a bistable arch, J. Mech. Phys. Solids 179 (2023) 105366, https://doi.org/10.1016/j.jmps.2023.105366.

[22] F. Dadgar-Rad, M. Hossain, Finite deformation analysis of hard-magnetic soft materials based on micropolar continuum theory, Int. J. Solids Struct. 251 (2022) 111747, https://doi.org/10.1016/j.ijsolstr.2022.111747.

[23] R. Zhang, S. Wu, Q. Ze, R. Zhao, Micromechanics study on actuation efficiency of hard-magnetic soft active materials, J. Appl. Mech. 87 (2020) 091008, https://doi.org/10.1115/1.4047291.

[24] D. Garcia-Gonzalez, M. Hossain, A microstructural-based approach to model magneto-viscoelastic materials at finite strains, Int. J. Solids Struct. 208–209 (2021) 119–132, https://doi.org/10.1016/j.ijsolstr.2020.10.028.

[25] D. Garcia-Gonzalez, M. Hossain, Microstructural modelling of hard-magnetic soft materials: dipole–dipole interactions versus Zeeman effect, Extreme Mech. Lett. 48 (2021) 101382, https://doi.org/10.1016/j.eml.2021.101382.

[26] H. Ye, Y. Li, T. Zhang, Magttice: a lattice model for hard-magnetic soft materials, Soft Matter 17 (2021) 3560–3568, https://doi.org/10.1039/D0SM01662D.

[27] D. Mukherjee, M. Rambausek, K. Danas, An explicit dissipative model for isotropic hard magnetorheological elastomers, J. Mech. Phys. Solids 151 (2021) 104361, https://doi.org/10.1016/j.jmps.2021.104361.

[28] D. Mukherjee, K. Danas, A unified dual modeling framework for soft and hard magnetorheological elastomers, Int. J. Solids Struct. 257 (2022) 111513, https://doi.org/10.1016/j.ijsolstr.2022.111513.

[29] D. Garcia-Gonzalez, T. Ter-Yesayants, M.A. Moreno-Mateos, M.L. Lopez-Donaire, Hard-magnetic phenomena enable autonomous self-healing elastomers, Compos. Part B Eng. 248 (2023) 110357, https://doi.org/10.1016/j.compositesb.2022.110357.

[30] X. Li, W. Yu, J. Liu, X. Zhu, H. Wang, X. Sun, J. Liu, H. Yuan, A mechanics model of hard-magnetic soft rod with deformable cross-section under three-dimensional large deformation, Int. J. Solids Struct. 279 (2023) 112344, https://doi.org/10.1016/j.ijsolstr.2023.112344.

[31] L. Wang, Y. Kim, C.F. Guo, X. Zhao, Hard-magnetic elastica, J. Mech. Phys. Solids 142 (2020) 104045, https://doi.org/10.1016/j.jmps.2020.104045.

[32] A. Rajan, A. Arockiarajan, Bending of hard-magnetic soft beams: a finite elasticity approach with anticlastic bending, Eur. J. Mech. A Solids 90 (2021) 104374, https://doi.org/10.1016/j.euromechsol.2021.104374.

[33] W. Chen, L. Wang, Theoretical modeling and exact solution for extreme bending deformation of hard-magnetic soft beams, J. Appl. Mech. 87 (2020) 041002, https://doi.org/10.1115/1.4045716.

[34] W. Chen, Z. Yan, L. Wang, Complex transformations of hard-magnetic soft beams by designing residual magnetic flux density, Soft Matter 16 (2020) 6379–6388, https://doi.org/10.1039/C9SM02529D.

[35] W. Chen, Z. Yan, L. Wang, On mechanics of functionally graded hard-magnetic soft beams, Int. J. Eng. Sci. 157 (2020) 103391, https://doi.org/10.1016/j.ijengsci.2020.103391.

[36] F. Dadgar-Rad, M. Hossain, Large viscoelastic deformation of hard-magnetic soft beams, Extreme Mech. Lett. 54 (2022) 101773, https://doi.org/10.1016/j.eml.2022.101773.

[37] A.M. Dehrouyeh-Semnani, On bifurcation behavior of hard magnetic soft cantilevers, Int. J. Non-Linear Mech. 134 (2021) 103746, https://doi.org/10.1016/j.ijnonlinmec.2021.103746.

[38] W. Chen, L. Wang, Z. Yan, B. Luo, Three-dimensional large-deformation model of hard-magnetic soft beams, Compos. Struct. 266 (2021) 113822, https://doi.org/10.1016/j.compstruct.2021.113822.

[39] T.G. Sano, M. Pezzulla, P.M. Reis, A Kirchhoff-like theory for hard magnetic rods under geometrically nonlinear deformation in three dimensions, J. Mech. Phys. Solids 160 (2022) 104739, https://doi.org/10.1016/j.jmps.2021.104739.

[40] F. Dadgar-Rad, A. Hemmati, M. Hossain, A three-dimensional micropolar beam model with application to the finite deformation analysis of hard-magnetic soft beams, Int. J. Solids Struct. 290 (2024) 112662, https://doi.org/10.1016/j.ijsolstr.2024.112662.

[41] W. Chen, L. Wang, Z. Yan, On the dynamics of curved magnetoactive soft beams, Int. J. Eng. Sci. 183 (2023) 103792, https://doi.org/10.1016/j.ijengsci.2022.103792.

[42] A.M. Dehrouyeh-Semnani, Nonlinear geometrically exact dynamics of fluid-conveying cantilevered hard magnetic soft pipe with uniform and nonuniform magnetizations, Mech. Syst. Signal Process. 188 (2023) 110016, https://doi.org/10.1016/j.ymssp.2022.110016.

[43] W. Huang, M. Liu, K.J. Hsia, A discrete model for the geometrically nonlinear mechanics of hard-magnetic slender structures, Extreme Mech. Lett. 59 (2023) 101977, https://doi.org/10.1016/j.eml.2023.101977.

[44] W. Huang, M. Liu, K.J. Hsia, Modeling of magnetic cilia carpet robots using discrete differential geometry formulation, Extreme Mech. Lett. 59 (2023) 101967, https://doi.org/10.1016/j.eml.2023.101967.

[45] A. Borković, B. Marussig, G. Radenković, Geometrically exact static isogeometric analysis of an arbitrarily curved spatial Bernoulli–Euler beam, Comput. Methods Appl. Mech. Eng. 390 (2022) 114447, https://doi.org/10.1016/j.cma.2021.114447.

[46] E. Reissner, On one-dimensional finite-strain beam theory: the plane problem, Z. Für Angew. Math. Phys. ZAMP 23 (1972) 795–804, https://doi.org/10.1007/BF01602645.

[47] J.C. Simo, A finite strain beam formulation. The three-dimensional dynamic problem. Part I, Comput. Methods Appl. Mech. Eng. 49 (1985) 55–70, 10/cvb8rf.

[48] J.C. Simo, L. Vu-Quoc, A three-dimensional finite-strain rod model. Part II: computational aspects, Comput. Methods Appl. Mech. Eng. 58 (1986) 79–116, 10/b8wd4z.

[49] M.A. Crisfield, G. Jelenić, Objectivity of strain measures in the geometrically exact three-dimensional beam theory and its finite-element implementation, Proc. R. Soc. Lond. Ser. Math. Phys. Eng. Sci. 455 (1999) 1125–1147, https://doi.org/10.1098/rspa.1999.0352.

[50] F. Armero, J. Valverde, Invariant Hermitian finite elements for thin Kirchhoff rods. I: the linear plane case, Comput. Methods Appl. Mech. Eng. 213–216 (2012) 427–457, https://doi.org/10.1016/j.cma.2011.05.009.

[51] F. Armero, J. Valverde, Invariant Hermitian finite elements for thin Kirchhoff rods. II: the linear three-dimensional case, Comput. Methods Appl. Mech. Eng. 213–216 (2012) 458–485, https://doi.org/10.1016/j.cma.2011.05.014.

[52] C. Meier, A. Popp, W.A. Wall, An objective 3D large deformation finite element formulation for geometrically exact curved Kirchhoff rods, Comput. Methods Appl. Mech. Eng. 278 (2014) 445–478, https://doi.org/10.1016/j.cma.2014.05.017.

[53] X. Li, W. Yu, M. Baghaee, C. Cao, D. Chen, J. Liu, H. Yuan, Geometrically exact finite element formulation for tendon-driven continuum robots, Acta Mech. Solida Sin. (2022), https://doi.org/10.1007/s10338-022-00311-w.

[54] E. Reissner, On finite deformations of space-curved beams, ZAMP Z. F?r Angew. Math. Phys. 32 (1981) 734–744, https://doi.org/10.1007/BF00946983.

[55] R.K. Kapania, J. Li, On a geometrically exact curved/twisted beam theory under rigid cross-section assumption, Comput. Mech. 30 (2003) 428–443, https://doi.org/10.1007/s00466-003-0421-8.

[56] A. Borković, S. Kovačević, G. Radenković, S. Milovanović, M. Guzijan-Dilber, Rotation-free isogeometric analysis of an arbitrarily curved plane Bernoulli–Euler beam, Comput. Methods Appl. Mech. Eng. 334 (2018) 238–267, https://doi.org/10.1016/j.cma.2018.02.002.

[57] G. Radenković, A. Borković, Linear static isogeometric analysis of an arbitrarily curved spatial Bernoulli–Euler beam, Comput. Methods Appl. Mech. Eng. 341 (2018) 360–396, https://doi.org/10.1016/j.cma.2018.07.010.

[58] A. Borković, S. Kovačević, G. Radenković, S. Milovanović, D. Majstorović, Rotation-free isogeometric dynamic analysis of an arbitrarily curved plane Bernoulli-Euler beam, Eng. Struct. 181 (2019) 192–215, https://doi.org/10.1016/j.engstruct.2018.12.003.

[59] G. Radenković, A. Borković, On the analytical approach to the linear analysis of an arbitrarily curved spatial Bernoulli–Euler beam, Appl. Math. Model. 77 (2020) 1603–1624, https://doi.org/10.1016/j.apm.2019.09.012.

[60] A. Borković, B. Marussig, G. Radenković, Geometrically exact static isogeometric analysis of arbitrarily curved plane Bernoulli–Euler beam, Thin-Walled Struct 170 (2022) 108539, https://doi.org/10.1016/j.tws.2021.108539.

[61] K. Tan, L. Chen, S. Yang, Q. Deng, Dynamic snap-through instability and damped oscillation of a flat arch of hard magneto-active elastomers, Int. J. Mech. Sci. 230 (2022) 107523, https://doi.org/10.1016/j.ijmecsci.2022.107523.

[62] K.-J. Bathe (Ed.), Finite Element Procedures, 2nd ed., K.J. Bathe, Watertown, MA, 2014.

[63] J.C. Simo, L. Vu-Quoc, On the dynamics in space of rods undergoing large motions — A geometrically exact approach, Comput. Methods Appl. Mech. Eng. 66 (1988) 125–161, 10/frsw25.